University of São Paulo

Institute of Astronomy, Geophysics and Atmospheric Science

Department of Geophysics

José Alexandre Araújo Nogueira

Relative Location of Regional Epicenters in Brazil and Source Parameters

São Paulo

2023

José Alexandre Araújo Nogueira

Relative Location of Regional Epicenters in Brazil and Source Parameters

Dissertation presented at the Institute of Astronomy, Geophysics and Atmospheric Sciences at the University of São Paulo as a partial requirement for obtaining the title of Master of Science.

Area of concentration: Geophysics
Orientador: PhD. Marcelo Sousa de Assumpção

São Paulo

2023

To my family and friends

Acknowledgements

"A minhoca pediu à Terra, e esta lhe abriu a boca"

Autor desconhecido

Resumo

Utilizamos a análise de correlação cruzada das ondas P, S e Lg para localizar com precisão as réplicas de um terremoto em relação a um evento de referência. Ao analisar a distribuição das réplicas em diversos casos, pudemos inferir parâmetros da fonte, como o plano de falha do terremoto principal, estimar o *stress drop* e fornecer restrições para a determinação do mecanismo focal. A metodologia envolve duas abordagens que requerem um sismo referência e um alvo, cujos sinais são correlacionados a fim de obter os tempos de percurso relativos para uma estação. Essa metodologia auxiliou na estimativa das características da fonte de quatro sequências de sismos na região intraplaca brasileira. De forma geral, todos os eventos foram relocados para mais próximos ao evento referência. Especificamente, os resultados mostram um padrão de falha NW-SE e um mecanismo focal reverso para as sequências de Amargosa-BA (2018-2020) e Cajati-SP (2015-2020). Os terremotos de 1965 e 2021 na Guiana não tiveram origem na mesma falha. A sequência de Sete Lagoas-MG (Abr-Dez/2022) apresentou duas possibilidades: ocorrência de sismos em planos independentes ou uma tendência SW-NE mergulhando para o NW.

Palavras-chave: Localização relativa, Epicentro, Falha, Mecanismo focal.

Abstract

We employed cross-correlation analysis of P, S, and Lg-waves to accurately locate the aftershocks relative to a reference event. By analyzing the distribution of aftershocks in several cases, we were able to infer the source parameters like fault plane of the main earthquake, stress drop characteristics and provide constraints for the focal mechanism determination. The methodology involves two approaches that requires a reference event whose signals are cross-correlated with another event (target) to obtain relative travel times to a given regional network. This method assisted in estimating the source characteristics of four seismic Mainshock-aftershock sequences in intraplate region of Brazil. In general, all events were relocated near the mainshock. Specifically, the results show a NW-SE fault trend and thrust focal mechanism for Amargosa-BA (2018-2020) and Cajati-SP (2015-2020) sequences. The 1965 and 2021 earthquakes in Guyana did not originate from the same fault. The Sete Lagoas-MG (Apr-Dec/2022) sequence exhibited two possibilities: either independent fault planes or a SW-NE trend dipping to NW.

Keywords: Relative location, Epicenter, Fault, Focal mechanism.

List of Figures

List of Tables

Contents

Chapter 1

Introduction

The location of seismic events is traditionally performed based on the first arrivals of P, S-waves. Regardless of low signal-to-noise ratio (SNR), even when the phases are accurately determined, the epicentral error can reach several kilometers due to the lack of azimuthal control and unpredicted heterogeneities in the simplistic 1D velocity model.

According to Bondár et al. (2004), the use of regional stations for absolute epicentral location can result in uncertainties of up to 20 km. However, to achieve errors below 5 km, it is crucial to have a minimum of 10 stations within a 200 km radius of the epicenter. The limited number of seismic stations in low-seismicity regions, such as Brazil, poses challenges in accurately determining epicentral locations.

Fig. 1.1 illustrates an example of absolute location for the Sete Lagoas-MG sequence. The plotted epicenters here are preliminary determinations from the catalog of the University of São Paulo Seismological Center. The epicenters are distributed in an area with radius of 5km and have similar waveforms, with cross-correlation coefficient, (CC) > 0.70, which is considered high based on SNR for regional seismic network (> 100 km).

Upon examining **Fig. 1.1**, the sparse distribution of the absolute location, is not consistent with the waveform correlation displayed between the sequence **Fig. 1.2**. Furthermore, high waveform similarity between events is often observed when they share similar propagation paths and focal mechanisms (Chiu and Snyder, 2015).
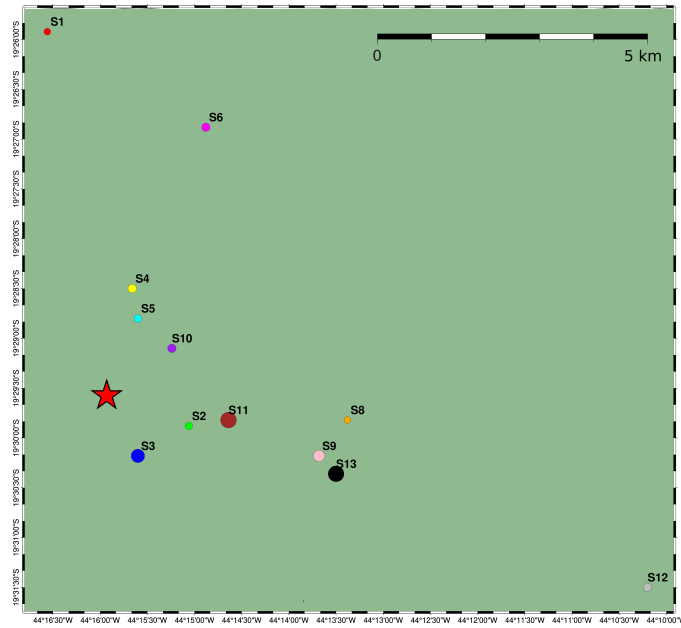
Figure 1.1: Absolute location was performed by the USP Seismological Center using regional stations. The aftershocks exhibit an sparsity distribution (colored circles, mR 2.0-2.9) and are located approximately 1km or more away from the main event (red star, mR 2.9).
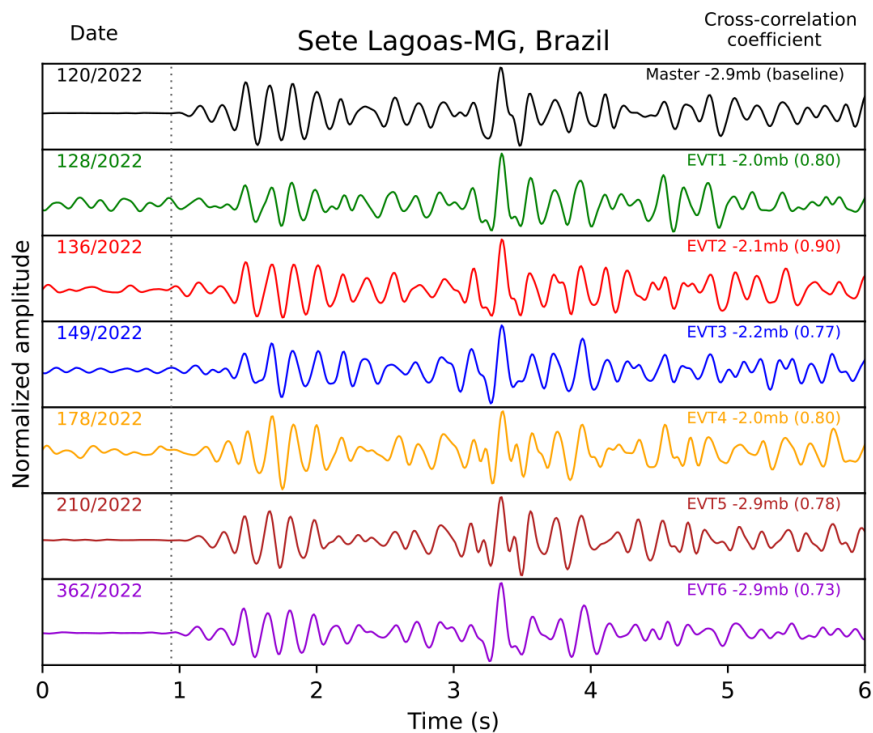
Figure 1.2: Example of almost identical waveforms between earthquake occurrence in Sete Lagoas-MG (Brazil). The waveforms recorded by the BL.DIAM station located at a distance of 145km, represent the vertical component of velocity, filtered with a band-pass filter ranging from 2Hz to 8Hz. The date and magnitude and cross correlation coefficient of the event are displayed in the upper corners.

This discrepancy between the observed earthquake locations and the expected geographical proximity based on waveform similarity raises questions about the accuracy of locations with a regional seismic network. Moroever, aftershocks of a seismic series typically occur in proximity and sometimes, they can be associated with the fault plane of the main earthquake. Thus, aftershocks could potentially offer valuable insights into the fault area of the mainshock, stress drop characteristics and provide constraints for the focal mechanism determination (**Fig. 1.3**). Based on that, the aftershock area has been extensively utilized as an approximation for the fault area of the mainshock (Das and Henry, 2003), (Ciardelli and Assumpção, 2019), (Waldhauser et al., 2021).
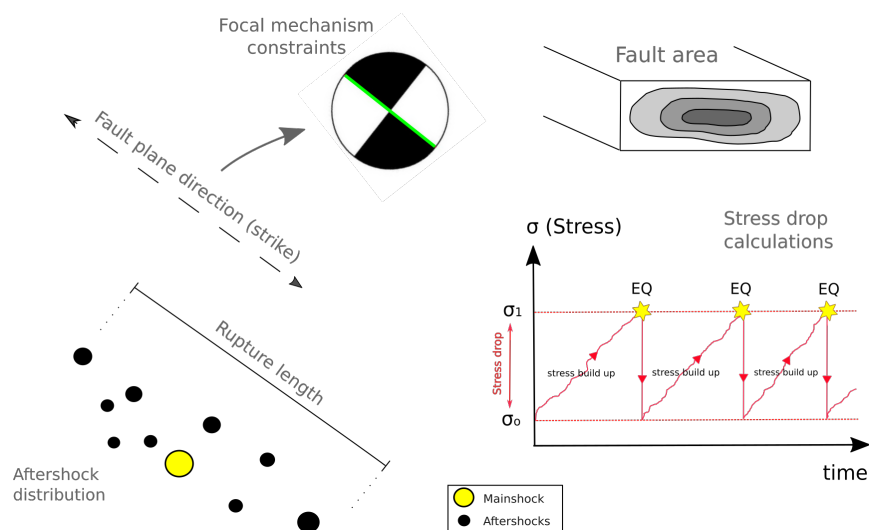
Figure 1.3: Schematic figure illustrating the information that aftershocks can provide, like rupture length, fault orientation (strike), fault area and stress drop.

However, as demonstrated by studies conducted by Gao et al. (2021), waveform similarity alone is not the most effective way to determine which events occurred on the same fault plane. The optimal procedure relies on the overlap of the source areas (Waldhauser and Ellsworth, 2002). Nonetheless, this approach requires a precise assessment of the interevent distance.

To better discriminate between on- or off-fault seismicity and the source characteristics that aftershocks can provide, rather than emphasizing absolute estimates of earthquake locations, an alternative practice is to improve relative estimates. Relative-location methods are based on the premise that when two earthquakes occur near each other, the paths from the source to a shared station will be nearly identical. Any differences in travel times can be attributed to the relative locations of the earthquakes, rather than unknown variations

in the heterogeneity between the source and receiver (Howe et al., 2019).

Our contribution to the study of intraplate earthquakes involves measuring some source parameters. This is accomplished by cross-correlating the P, S, and Lg-wave signals of all aftershocks recorded at each station and combining Rayleigh wave time shifts with station corrections. This methodology will assist in estimating the fault geometry of four seismic Mainshock-aftershock sequences (**Fig.** 1.4) in intraplate region of Brazil, and infer the rupture area, focal mechanism and stress drop.
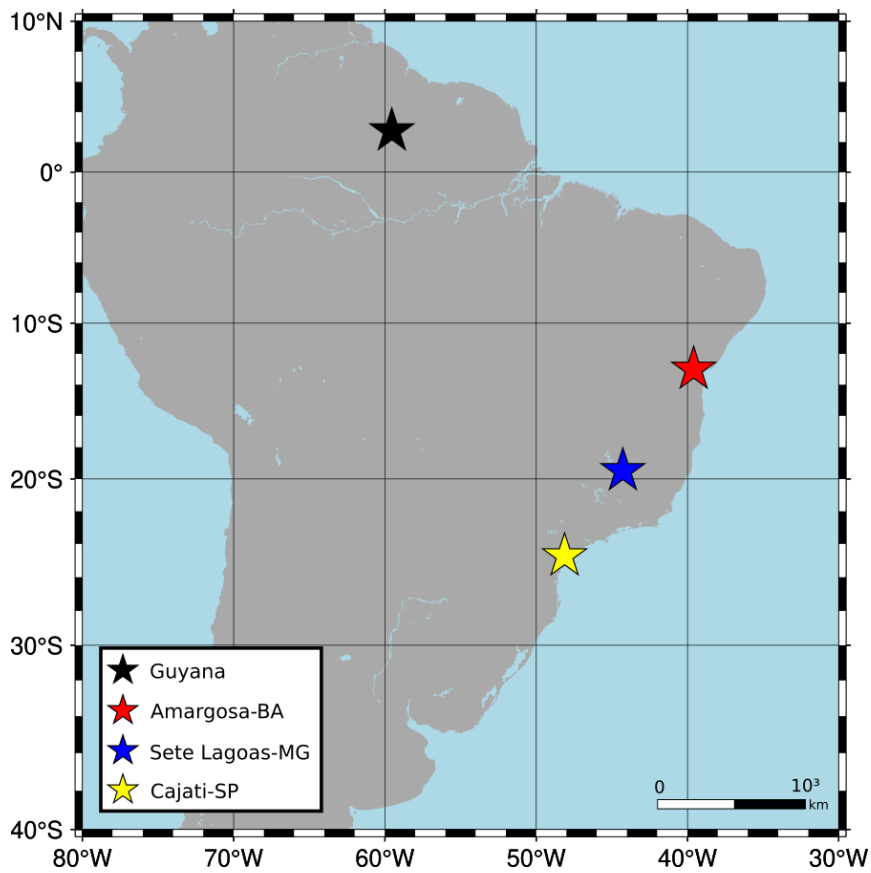
Figure 1.4: Map showing the events under investigation in this study.

Chapter 2

Methods

We will employ two independent methods for determining relative earthquake locations. Both methods act like stations corrections, wich uses the residual of the reference (or master event) as correction for lateral heterogeneities. As a consequence of that, the technique accounts for velocity anomalies and lateral contrasts, resulting in more accurate relative locations. Although both methods serve as station corrections, in order to differentiate them, we will use the term "station correction" when referring to the first method (section 2.1), and "Rayleigh time shift" or "sinusoidal time shift" when referring to the second method (section 2.2).

2.1 Station correction method

First, the reference event is located absolutely using an average velocity model for Brazil, by Assumpção et al. (2010). Then, we correlate the P, S, and Lg-waves between the reference and target events for precise adjustment in the pick times. The residuals from the absolute location of the reference earthquake in the series are used as station corrections for the targets, and a new location and origin time are determined. This technique is widely used and has been successfully applied in previous studies (Assumpção et al., 2016), (Rivadeneyra-Vera et al., 2016), (Ciardelli and Assumpção, 2019), (Waldhauser, 2000).

The relative location of an event requires a velocity model and determining the arrival times of P and S-waves. Assuming that the reference event is well-located, it is possible to calculate the difference between the observed arrival times and the predicted times based on the velocity model. This discrepancy is known as the residual time or residual,

represented by $t_{res} = t_{obs} - t_{pred}$, and it is calculated individually for each seismographic station.

The residuals calculated for the reference event (mainshock of the sequence, usually the largest magnitude event) are used as "station corrections" for all its aftershocks (target events) by subtracting this residual time (t_{res}) from the arrival time of the aftershocks. This method compensates for possible lateral velocity variations that are not accounted for the 1D velocity models, providing more precise relative location of these subsequent earthquakes.

For this purpose, we used the HYPOSAT software (Schweitzer, 2001), which incorporates body and surface waves. The HYPOSAT software, can be considered as an aplication and refinement of the Geiger (1910) inversion method for seismic location. The Geiger method is a seismic location technique that utilizes the arrival times of seismic waves recorded at multiple stations to determine the location of an earthquake.

The procedure for applying the "station correction method", in this study, can be summarized as follows:

(step 1): Choose one event as a reference and others as targets and read the arrival times for body and surface waves.

(step 2): In pairs, correlate the waveform between the reference event and each target event to refine the picks.

(step 3): Assuming that the reference event is well-located, calculate its residual ($t_{res} = t_{obs} - t_{pred}$) based on the NewBR velocity model (Assumpção et al., 2010).

(step 4): Use the calculated residual from the reference event to correct the arrival times for the targets.

(step 5): With the corrected arrival time, calculate the new location for the targets.

2.2   Rayleigh time shift or sinusoidal time shift method

The second technique, proposed by Von Seggern (1972), determine the relative locations of seismic events by cross-correlation of surface-wave signals to obtain the differential travel times between events recorded at the same stations.

Compared to body waves, surface waves often have a higher SNR, which is crucial for

low-magnitude events recorded at regional distances. Another advantage is the low propagation velocity of surface waves, which contributes to their high sensitivity to location. As an example, consider that the velocity of a regional P-wave is approximately 7 km/s, while a typical intermediate period Rayleigh wave has a phase velocity of approximately 3.5 km/s. This substantial difference indicates that a location difference of 7 km can lead to a shift of approximately 2 seconds in the surface waveform. In contrast, the P-wave experiences a much smaller shift of only about 1.0 second. A significant number of studies have taking advantage of these characteristics, such as Ekström (2006) , Barros et al. (2009), Michael Cleveland and Ammon (2013), Rivadeneyra-Vera et al. (2016), Assumpção et al. (2016), Ciardelli and Assumpção (2019). We use this method with three sequences of earthquakes in Brazil with mainshock magnitudes varying from 2.9 to 4.2 mR.

In the following lines, we will derive the equation used for the study. **Fig. 2.1** shows the basic geometry to locate a target event relative to a reference event, using the Lg waves.
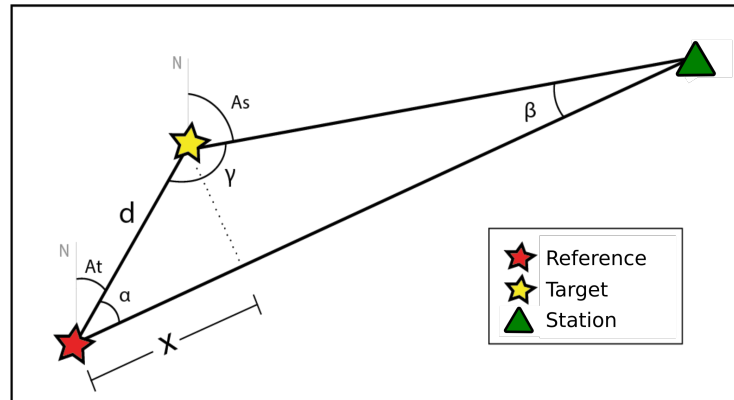
Figure 2.1: Geometry for relative location using Lg waves. The red star represents the reference event ("Master"); the yellow star represents the target event (epicenter to be determined) at a distance (d) and relative azimuth to the reference (A_t). The green triangle represents a station where Lg waves are correlated and the time shift is measured. The distance (d) between the events is much smaller than the distance to the station, which allows for the approximation of the angle $\beta \approx 0$.

Let the sum of the interior angles of triangle, denoted as $\overline{ABC}$, be $\alpha + \beta + \gamma = 180^o$. And also the sum of $(A_s - A_t) + \gamma = 180^o$.

Now, we can set up the following system of two equations:

$$\begin{cases} \alpha + \gamma + \beta & = 180^o \\ (A_s - A_t) + \gamma & = 180^o \end{cases}$$

Solving the linear system for α, we get

$$\alpha = A_s - A_t - \beta$$

And considering the far-station approximation, we can take the limit as $\beta \to 0$, then we find

$$\lim_{\beta \to 0} \alpha = A_s - A_t \tag{2.1}$$

Observing the travel times between the reference event and the target one, we obtain the equation

$$t_r - t_t = \frac{x}{c}$$

where t_t is the travel time of the target and t_r the travel time of the reference. Adding a correction A_o for the t_r term, relative to a possible origin time error of the target, we found

$$t_t - t_r = A_o - \frac{x}{c} \tag{2.2}$$

As we know that $x = d \cos(\alpha)$, with α given by Eq. (2.1), we have

$$\boxed{t_t - t_r = A_o - \frac{d}{c} \cos(A_s - A_t)} \tag{2.3}$$

The matrix formulation of equation Eq. (2.3) can be given by

$$\begin{bmatrix} T_1 \\ T_2 \\ \vdots \\ T_n \end{bmatrix} = \begin{bmatrix} 1 & x_1 \\ 1 & x_2 \\ \vdots & \vdots \\ 1 & x_n \end{bmatrix} \cdot \begin{bmatrix} A_o \\ -d \end{bmatrix} \tag{2.4}$$

Where $T_i = t_t^i - t_r^i$ and $x_i = \frac{1}{c} \cos(A_s^i - A_t)$.

Each index refers to the observed data from station i . For example, the station BOAV located in Boa Vista-RO has an arrival time difference T_1 and an x_1 calculated by the azimuth A_s^1 relative to the epicenter of the target earthquake (**Fig. 2.1**).

By the least squares method, the two parameters in matrix Eq. (2.4) can be find out by

$$\vec{m} = (G^T G)^{-1} G^T \vec{D}$$

Where $\vec{m}$ is the parameter vector, G is the sensitivity matrix, and $\vec{D}$ is the data vector.

One of the parameters A_t was included in the sensitivity matrix G because it couldn't be isolated in a parameter vector like we did with A_o and d. Nonetheless, we will still be able to determine it, by trial and error, using a step of 1 degree ($A_t = 0^o$ to 360°). For each tested angle A_t, we will have a pair of parameters as a solution, resulting in a total of 360 parameter pairs. In order to select among the 360 candidates, we will choose the parameter trio that best fits the observed data, meaning the one with the lowest root mean square (RMS) error.

2.2.1 Uncertainties calculation

The uncertainties of the inverted parameters in the vector $\vec{m}$ can be propagated using the covariance matrix

$$[cov(\vec{m})] = \sigma_o^2 (G^T G)^{-1} \tag{2.5}$$

Assuming σ_o as the standard deviation of the time shift measurements, it was adjusted based on the waveform correlation stability when shifting the correlation window and applying filtering. If the pick adjustment remains consistent, σ_o is low. However, if it varies, the standard deviation increases. In most cases, we observed good stability, and a value of $\sigma_o = 0.03$ is being used as a benchmark.

Using the covariance matrix, we calculate the uncertainties of the two parameters ($d \pm \sigma_d$) and ($A_o \pm \sigma_{A_o}$). Now, we will propagate these uncertainties to the estimated parameter A_t through the least squares equation, that is, we can determine A_t uncertainties based on the uncertainties and values of the inverted parameters, i.e. A_o and d. The uncertainties propagation is described by a differential equation

$$\sigma_{A_t} = \sqrt{(\frac{\partial A_t}{\partial d})^2 . (\sigma_d)^2 + (\frac{\partial A_t}{\partial A_o})^2 . (\sigma_{A_o})^2} \tag{2.6}$$

In which A_t is isolated from Eq. (2.3), which give

$$A_t = A_t(A_o, d) = A_s - \arccos\left(\frac{c.(A_o - T_i)}{d}\right)$$

For each measurement $t_t^i - t_r^i = T_i$, for $(i = 1, 2, 3, 4, ..., n)$, we will have n values of σ_{A_t}, which will be represented by the average.

Now, with Eq. (2.5) and (2.6) we can determine the uncertainties for both the inverted parameters d and A_o, as well as for the estimated parameter A_t, respectively.

Fig. 2.2 displays an example of fitting the sinusoidal curve between the main event of Amargosa (30/08/2020, 4.2mb, reference) and one of its aftershocks occurring 30 minutes after the main event, using the deduced method.
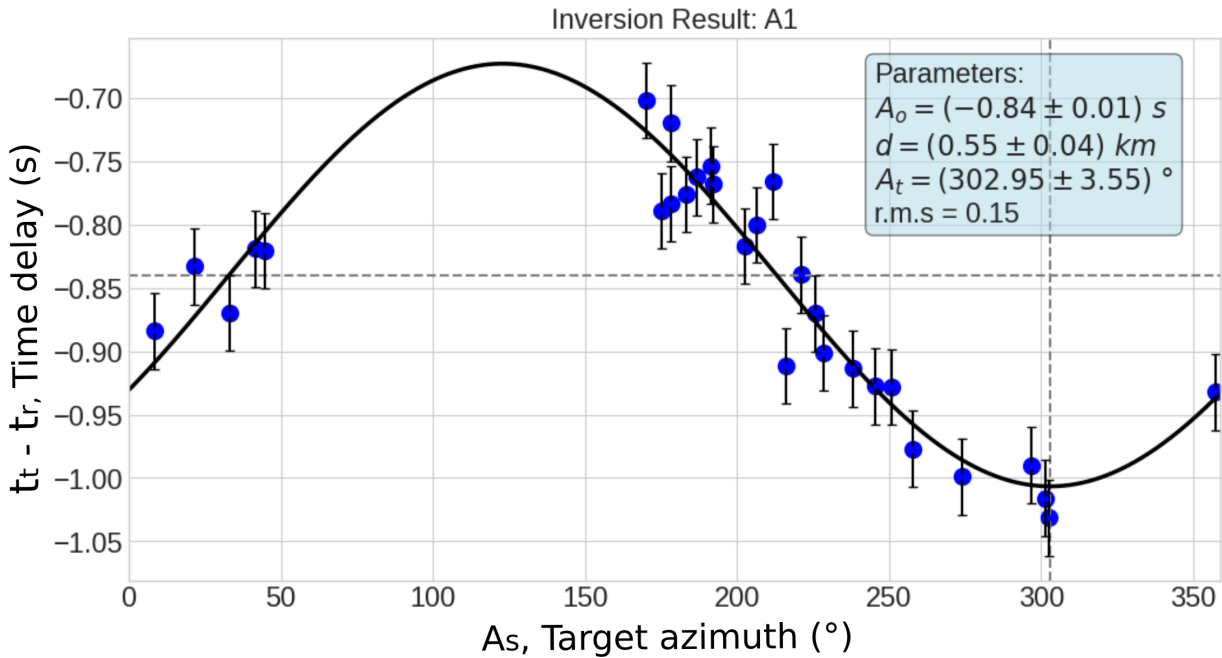
Figure 2.2: Example of fitted curve for the Lg relative location of the first aftershock of Amargosa (2020) event. Y-axis represents the time shift measurament $(t_t - t_r)$ and X-axis represents the station azimuth (A_s). A total of 30 station were utilized. The dark line are the curve fit, and the blue points means the time shift measurements with their associated uncertainty $\sigma_o = 0.03s$. The light blue box displays the inverted parameters and their errors.

Chapter 3

Guyana

The Guyana earthquake on January 31, 2021, was one of the largest intra-plate seismic events that happened in South America since 1955. The magnitude, as measured by the USP Seismology Center, was mb 6.0. According to the news and reports from the population through the monitoring platform of USP, the 2021 earthquake was felt in Roraima, Manaus, and Georgetown, capital of Guyana. Earthquake records in this region are not unprecedented. According to the Brazilian Seismic Bulletin (and the ISC bulletin), in the Roraima/Guyana border region, there have been two other earthquakes: in 1964 (mb 4.3) and 1965 (mb 4.8). In Boa Vista-RO, tremors were also felt in 1928 and 1953, but we have limited information about both events.

The two events studied here (1965 and 2021 mainshock) are located in the central region of the Guyana Shield (**Fig. 3.1**), wich corresponds to the northern part of the Amazon Craton. The study area belongs to the Tapajós-Parima Province (Santos et al., 2000), with ages ranging from 2.03 to 1.88 Ga. It is characterized by granitic rocks, high-grade metamorphic shield and siliciclastic sedimentary rocks, the latter occurring in the Takutu Basin.

The question arises as to whether the 1965 event could have occurred on the same seismogenic fault that ruptured in 2021, give that teleseismic locations in the 1960's had uncertainties of a few 10's of km. This question can be studied through the relative location between the 1965 earthquake and the 2021 earthquake. The goal here, is relocate the 2021 mainshock and the 1965 event. For this purpose, we used the HYPOCENTER software (Lienert and Havskov, 1995) for the determination of teleseismic epicenters, along with the regional velocity model for Brazil (Assumpção et al., 2010).
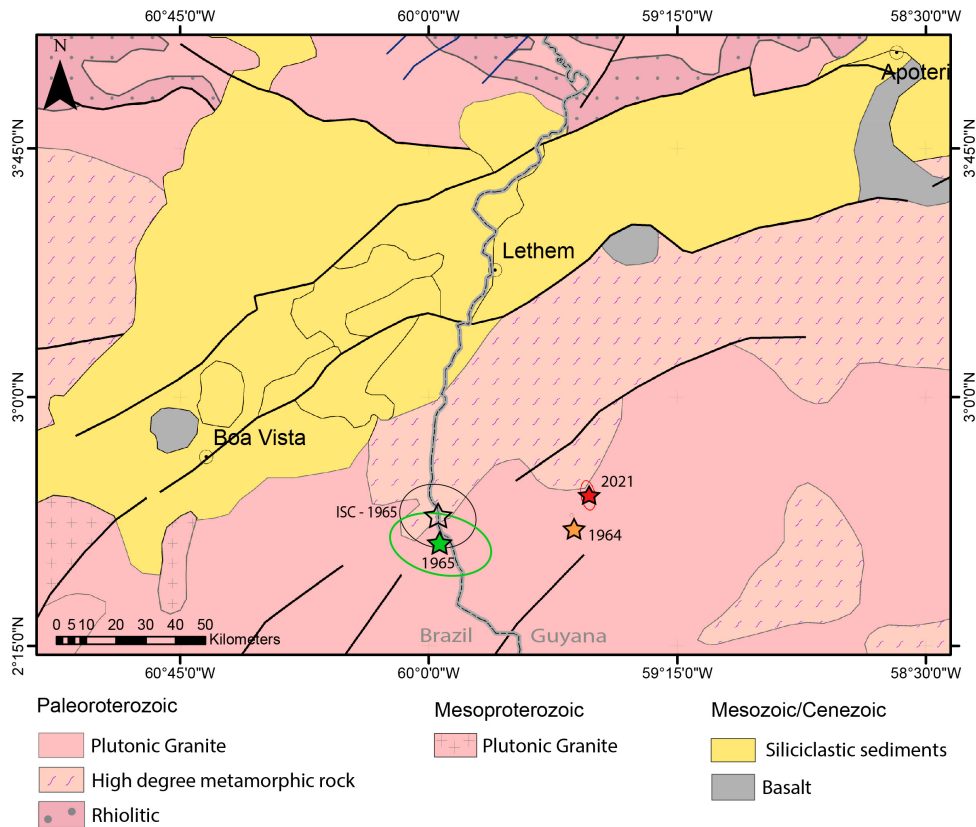
Figure 3.1: Epicenters of the 1965 (black open star: Located by the ISC; Green star: Relocated in this work), 1964 (orange star, ISC location) and 2021 events (red stars). Map background shows lithology from the Brazilian Geologic Survey (CPRM).

3.1   2021 mainshock relocation

The 2021 earthquake in Guyana was an unusual event, first because of its high magnitude in an intraplate region close to a sedimentary basin, and also because it was one of the few events fortunate enough to be recorded by InSAR satellites. **Fig. 3.2** shows the ground movement captured by Sentinel-1, which is part of Copernicus, the Earth observation component of the European Union Space Programme. The satellite utilizes a technique called Interferometric Synthetic Aperture Radar (InSAR), which provides detailed information on ground deformation. For more information about this technique, refer to Bürgmann et al. (2000). Given the scarcity of stations in this region, it would have been challenging to determine the position of the main tremor with such precision. Therefore, it is fortunate that we were able to achieve this level of accuracy.

One month after the mainshock, four local stations were installed by IAG-USP and the Geological Service of Guyana to locate the aftershocks. As a result, we have a well-located
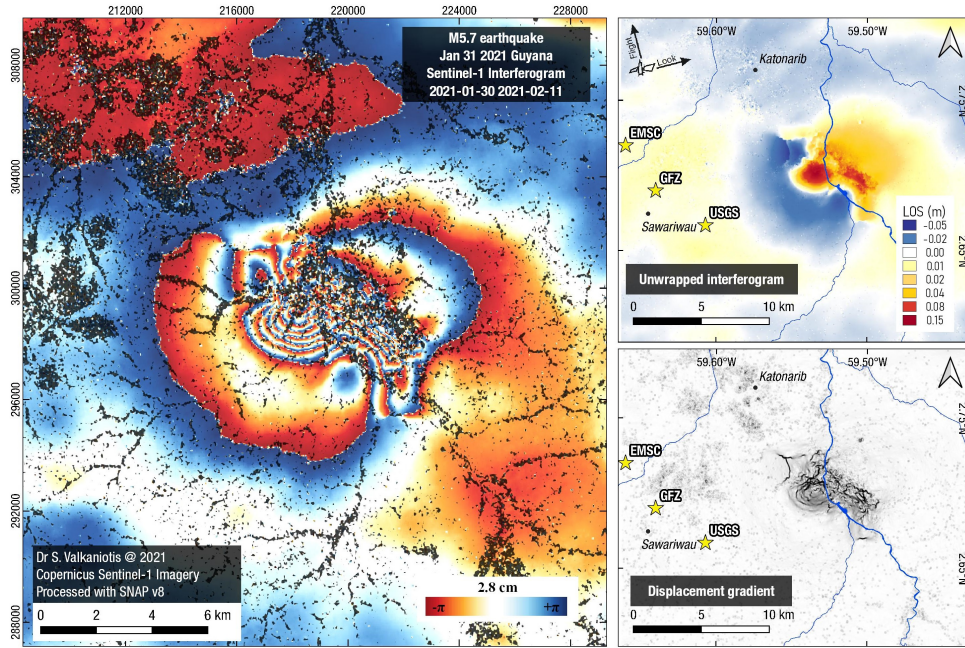
Figure 3.2: The Copernicus Sentinel-1 satellite captured an interferogram of the ground movement, showing a complex fault rupture striking in a northwest-southeast direction. With the use of InSAR, the absolute position of the earthquake can be estimated with great precision. On the figures to the right, we can see the locations results of some agencies, namely USGS, EMSC, and GFZ, with displacements of up to 10 km from the original epicenter.

dataset comprising the aftershocks (from the local stations) and the mainshock (from the Sentinel-1 radar). The unique circumstances of the Guyana case make it an excellent scenario to test the relative station correction method (section 2.1). In this chapter, we will utilize one of the largest and well-located aftershocks (mb 4.8, on 26/03/2021) as a reference for the relocation of the Guyana mainshock. Since we know the precise positions of both events, we want to check if the results align accordingly, i.e., we will use this well-located aftershock to determine the epicenter of the mainshock, and compare to the Sentinel-1 radar epicenter.

The common stations that recorded both events, the aftershock (reference) and the mainshock (target), are shown in **Fig. 3.3**. By fixing the epicenter and origin time of the reference, we obtained the residuals for each station (**Tab. 3.1**). The original arrival times for the target event and their location residuals are shown in **Tab. 3.2**. **Tab. 3.3** presents the final results of the target relocation with reduced residuals after the stations corrections.
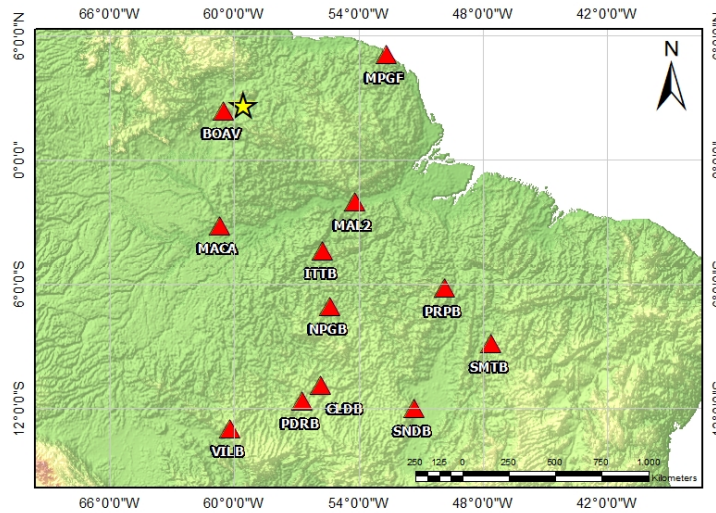
Figure 3.3: Yellow star shows location of Guyana 2021 earthquake sequence. Red triangles are stations used for relative location. All stations recorded both events: the main earthquake (target, mb 6.0) and the reference earthquake (largest aftershock, mb 4.8).

Table 3.1 - Arrival times and residuals per station for the well-located reference aftershock (mb 4.8) . The residual column will be used for correcting the arrival times per station for the target mainshock in 2021. Depth and location (loc) are indicated at the top of the table. "F"denotes fixed parameters.

Depth: 2.2km F	loc: 2.730 -59.550 F		1.9 rms
Station	Phase	Arrival (hh mm ss)	Residual
BOAV	EP	15 58 1.62	-1.09
BOAV	ES	15 58 14.97	-2.33
MACA	EP	15 59 12.18	-1.29
MACA	ES	16 0 19.38	-1.04
MAL2	EP	15 59 27.96	-1.76
MPGF	EP	15 59 28.76	-2.85
MPGF	ES	16 0 48.61	-3.38
ITTB	EP	15 59 39.23	-2.39
NPGB	EP	16 0 12.75	-3.94
PRPB	EP	16 0 47.14	-4.57
CLDB	EP	16 0 58.80	-4.79
PDRB	EP	16 1 5.45	-4.92
VILB	EP	16 1 19.87	-4.96
SMTB	EP	16 1 31.60	-6.48
SNDB	EP	16 1 33.25	-7.23

Table 3.2 - Arrival times and residuals for the 2021 mainshock without station correction

Depth: 0km F		loc: 2.739 -59.489	1.1 rms
Station	Phase	Arrival (hh mm ss)	Residual
BOAV	EP	19 5 32.69	0.82
BOAV	ES	19 5 46.31	-1.00
MACA	EP	19 7 49.19	1.47
MACA	ES	19 7 49.19	-0.18
MAL2	EP	19 6 58.99	1.54
MPGF	EP	19 6 59.75	0.69
MPGF	ES	19 8 18.25	-0.77
ITTB	EP	19 7 9.98	0.38
NPGB	EP	19 7 43.50	-1.24
PRPB	EP	19 8 17.73	-1.72
CLDB	EP	19 8 29.36	-2.40
PDRB	EP	19 8 35.84	-2.76
VILB	EP	19 8 49.66	-3.60
SMTB	EP	19 9 1.62	-4.23
SNDB	EP	19 9 3.96	-4.50

Table 3.3 - Location of the mainshock in 2021 (Target event, mb 6.0) after correcting the arrival times using the residuals from the reference event.

Depth: 0km F		loc: 2.704 -59.520	0.5 rms
Station	Phase	Arrival (hh mm ss)	Residual
BOAV	EP	19 5 33.78	-0.01
BOAV	ES	19 5 48.64	-0.02
MACA	EP	19 6 44.74	0.58
MACA	EP	19 7 50.23	-0.88
MAL2	EP	19 7 0.75	0.61
MPGF	EP	19 7 2.60	0.30
MPGF	ES	19 8 21.63	-1.05
ITTB	EP	19 7 12.37	0.30
NPGB	EP	19 7 47.44	0.28
PRPB	EP	19 8 22.30	0.17
CLDB	EP	19 8 34.15	0.05
PDRB	EP	19 8 40.76	-0.15
VILB	EP	19 8 54.62	-0.84
SMTB	EP	19 9 8.10	-0.41
SNDB	EP	19 9 11.19	0.25

The relocalized epicenter of the mainshock in 2021 agrees very well with the location obtained from InSAR data, especially using both, P and S phases (**Fig. 3.4**). The error in relative relocation is only a few meters. The distance between the relocated epicenter and its largest aftershock (mb 4.8) indicates that the 2021 fault has a NW-SE trend and spans approximately 5 kilometers, very similar to the fault trend observed by satellite data (**Fig. 3.2**). Furthermore, the relocation calculations (**Tab. 3.3**) show a reduction in the average residual of the stations compared to the traditional location shown in **Tab. 3.2**. This test with the 2021 mainshock shows that employing relative relocation with station residuals for corrections significantly enhanced the accuracy of estimated epicenters compared to the absolute location.
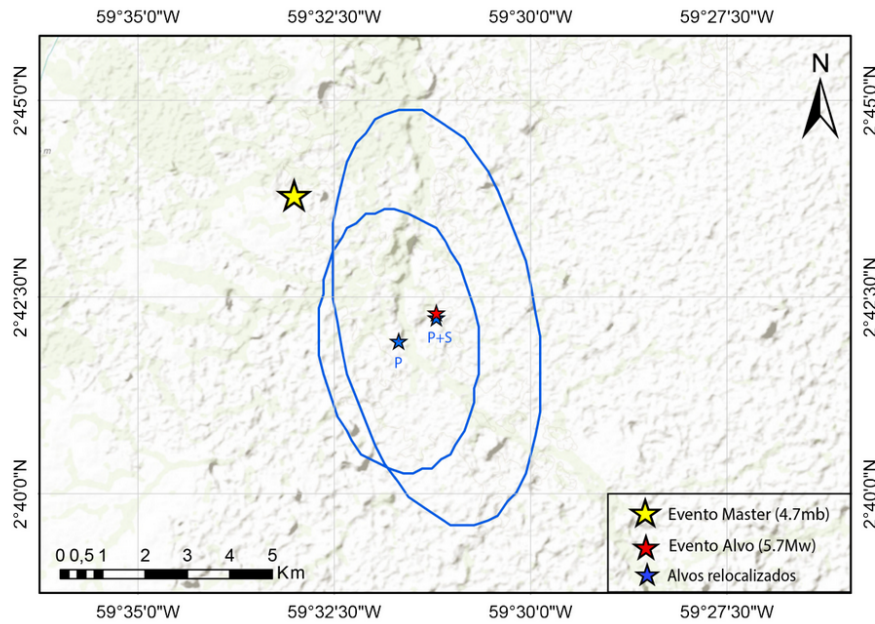
Figure 3.4: Mainshock of the 2021 series (2021-01-31, mb 6.0, target), located from the largest aftershock (2021-03-26, mb 4.8) used as a reference. Yellow Star is the reference epicenter determined by a local network. The red star is the location of the main event based on InSAR data. The two blue starts are the epicenters of the main event (target), relocated with station corrections, using only P arrivals or P+S arrivals.

3.2   1965 earthquake relocation

The 1965 earthquake occurred before the installation of the Brazilian Seismic Network (RSBR), and as a result, it was only located using distant international stations, leading to an imprecision of up to 50 km in the epicenter. This time, we are using the 2021 mainshock as a reference to relatively relocate the 1965 earthquake, their readings and epicenters are summarized in the ISC catalog, which is used in this study. For this purpose, we are using international stations that recorded both events. However, due to the long time elapsed, some stations have changed names or been repositioned. Therefore, we are using stations that have been repositioned within a range of up to 100 km from their original spot, the stations that recorded both events, the 1965 earthquake and the 2021 mainshock, are depicted in **Fig. 3.5**.

Tab. 3.4 shows the readings of arrival times and residuals for the 2021 earthquake at the stations that are common to the 1965 event. The arrival times for the mainshock of January 31, 2021 (reference) and the residuals obtained from the fixed epicenter at a
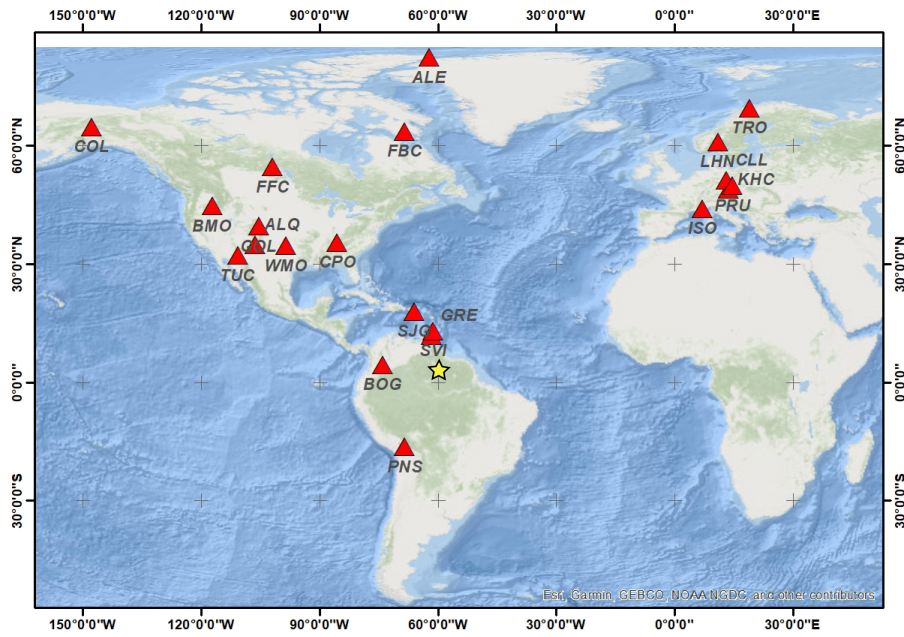
Figure 3.5: Common stations used for the relative location between the 1965 and 2021 earthquakes. Station names are the stations operating in 1965.

known location (InSAR data) are presented in **Tab. 3.5**. Finally, **Tab. 3.6** displays the results of the arrival times for the 1965 earthquake corrected by the residual of the 2021 mainshock, as well as their residuals in the relocation. A map showing the epicenters of the relative relocation of the 1965 earthquake is presented in **Fig. 3.6**.

Table 3.4 - Arrival times and residuals of the 2021 earthquake with a fixed hypocenter. The residual column will be used to correct the arrival times of the target earthquake of 1965. The second column shows the corresponding stations for the 1965 earthquake that are no longer operational.

Depth: 3km F		loc: 2.705 -59.520 F		1.1 rms
Station	sta	Phase	Arrival	Residue
GRGR	GRE	EP	19 7 32.30	-0.30
SVB	SVI	EP	19 7 45.30	-1.50
ROSC	BOG	EP	19 8 42.20	-3.59
SJG	SJG	EP	19 9 9.10	1.44
LPAZ	PNS	EP	19 9 56.80	1.04
LPAZ	PNS	ES	19 13 47.60	-1.70
U49A	CPO	EP	19 13 1.25	-0.43
WMOK	WMO	EP	19 13 56.12	-1.12
ANMO	ALQ	EP	19 14 39.51	-1.12
ISCO	GOL	EP	19 14 52.20	0.46
FRB	FBC	EP	19 15 30.00	-0.19
FFC	-	EP	19 15 36.11	-0.74
BMO	BMO	EP	19 15 59.50	-0.16
BNI	ISO	EP	19 16 36.29	0.81
KHC	-	EP	19 17 7.80	0.17
CLL	-	EP	19 17 8.40	0.42
PRU	-	EP	19 17 12.70	0.42
NOA	LHN	EP	19 17 16.20	0.47
ALE	-	EP	19 17 22.32	-0.92
TRO	-	EP	19 17 43.29	0.61
COLA	COL	EP	19 17 59.57	-0.15
QSP	SPA	EP	19 18 27.44	-0.30
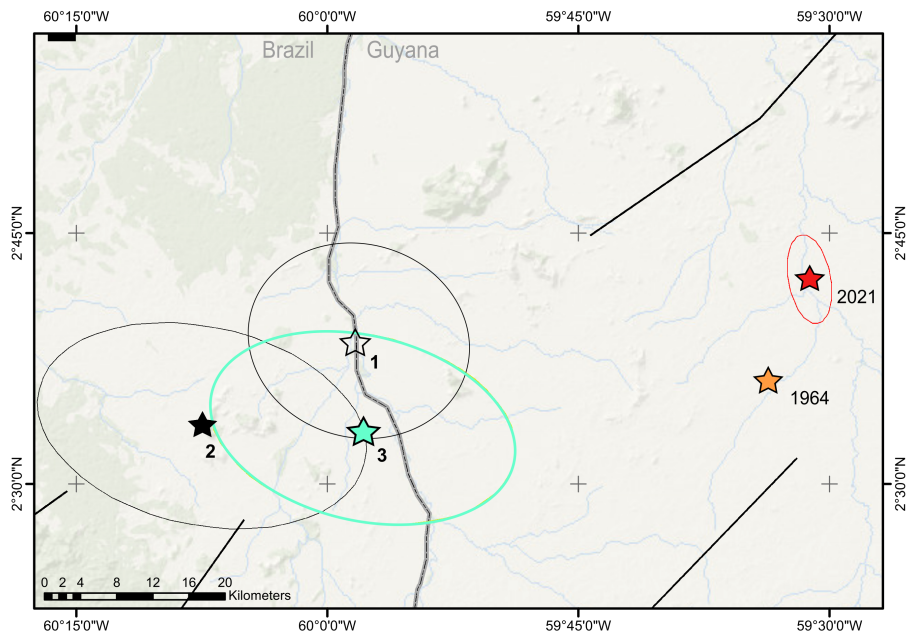
Figure 3.6: The epicenter numbers are, 1: Original location by ISC, 2: Traditional location for this work, 3: Relative location by the 2021 earthquake. Red and orange stars show the 2021 and 1964 earthquake respectively. Black lines correspond to regional faults by CPRM.

Table 3.5 - Arrival times and residuals of a location of the 1965 earthquake without station correction. Arrival times extracted from the ISC catalog.

Depth: 3km F		loc: 2.558 -60.125	1.4 rms
Station	Phase	Arrival (hh mm ss)	Residue
GRE	EP	19 39 8.00	-2.96
SVI	EP	19 39 23.00	-2.20
BOG	EP	19 40 15.00	2.18
SJG	EP	19 40 47.50	2.01
PNS	EP	19 41 33.70	1.93
PNS	ES	19 45 20.00	-2.89
CPO	EP	19 44 33.00	0.59
WMO	EP	19 45 32.00	-0.62
ALQ	EP	19 46 16.50	0.45
GOL	EP	19 46 27.30	0.36
TUC	EP	19 46 32.80	0.59
FBC	EP	19 47 09.00	-0.65
FFC	EP	19 47 14.00	-0.86
BMO	EP	19 47 36.00	-0.71
ISO	EP	19 48 18.90	1.24
KHC	EP	19 48 50.00	0.64
CLL	EP	19 48 50.00	0.37
PRU	EP	19 48 54.80	1.20
LHN	EP	19 48 56.70	0.65
ALE	EP	19 49 2.00	-0.93
TRO	EP	19 49 23.30	-0.07
COL	EP	19 49 37.90	-0.04
SPA	EP	19 50 5.50	-0.26

Table 3.6 - Location of the 1965 earthquake with arrival time correction using residuals from the reference event in Table 4. The depth was fixed at 3 km due to lack of resolution.

Depth: 3km F		loc: 2.556 -59.965	1.3 rms
Station	Phase	Arrival (hh mm ss)	Residue
GRE	EP	19 39 8.30	-2.97
SVI	EP	19 39 24.50	-0.88
BOG	EP	19 40 18.59	3.72
SJG	EP	19 40 46.06	-0.07
PNS	EP	19 41 32.66	0.31
PNS	ES	19 45 21.70	-2.33
CPO	EP	19 44 33.43	0.39
WMO	EP	19 45 33.12	-0.27
ALQ	EP	19 46 16.68	-0.14
GOL	EP	19 46 26.84	-0.78
TUC	EP	19 46 33.68	0.65
FBC	EP	19 47 09.19	-0.46
FFC	EP	19 47 14.74	-0.50
BMO	EP	19 47 36.16	-1.14
ISO	EP	19 48 18.09	1.19
KHC	EP	19 48 49.83	1.14
CLL	EP	19 48 49.58	0.59
PRU	EP	19 48 54.02	1.07
LHN	EP	19 48 56.23	0.69
ALE	EP	19 49 2.92	0.07
TRO	EP	19 49 22.69	-0.31
COL	EP	19 49 38.05	-0.13
SPA	EP	19 50 5.80	0.15

The relocalized epicenter of the 1965 earthquake is less than 20 km away from the original epicenter and remains significantly distant from the 2021 mainshock (**Fig. 3.6**). This indicates that the 1965 event did not occur on the same geological fault as the 2021 earthquake and is therefore an independent event.

From the lithogeological map (**Fig. 3.1**), we observe that the epicenters of the 1965, 1964, and 2021 earthquakes seem to form a SW-NE trending pattern, similar to the regional faults and basin boundary faults. However, as mentioned earlier, the 2021 event has a fault orientation of NW-SE. Therefore, this apparent alignment among the three events is not

significant.

Chapter 4

Amargosa sequence

The earthquake that occurred in Amargosa (BA) in 30 August 2020, with a magnitude of mR 4.2, was the strongest earthquake documented in the state of Bahia in the last 100 years. The region near the "Recôncavo Baiano" has a history of seismic activity, with a series of events occurring from 1911 to 1919. The largest events had magnitudes of up to 4.3 mb, including one in 1917 and another in 1919 (Berrocal et al., 1984).

The mainshock of 2020 had a regional magnitude (mR) of 4.2, but the International Seismological Centre (ISC) reported a teleseismic magnitude mb = 4.7. The waveform fitting conducted by this study, indicated a moment magnitude of Mw = 4.1.

The 30 August 2020 earthquake was strongly felt in the epicentral area, which includes cities such as Amargosa, Laje, Elísio Medrado, and Santo Antônio de Jesus. Reports from the "Sentiu Aí" website indicated that the tremors were felt by many people both inside and outside buildings and received extensive media coverage, with reports even coming from residents of tall buildings in Salvador-BA, located 120 km away. The RSBR regional stations recorded at least 17 events with a magnitude above mR 1.5. **Tab.** 4.1 shows the largest events that occurred near the Amargosa region from 2018 to 2021.

As shown in **Tab.** 4.1, the 2020 main event was followed by three additional events within a 1-hour interval, and a fourth event approximately 24 hours later. Two other events, in 2018 and 2019, with magnitudes > 3 mR had been previously recorded in the region. However, these events could be in a slightly different rupture in relation to the 2020 earthquake. **Fig.** 4.1, 4.2, 4.3, 4.4 and 4.5, show the waveform similarities among several stations that recorded these aftershocks. Additional figures from Amargosa S-waves correlation can be found in the Appendix (section A).
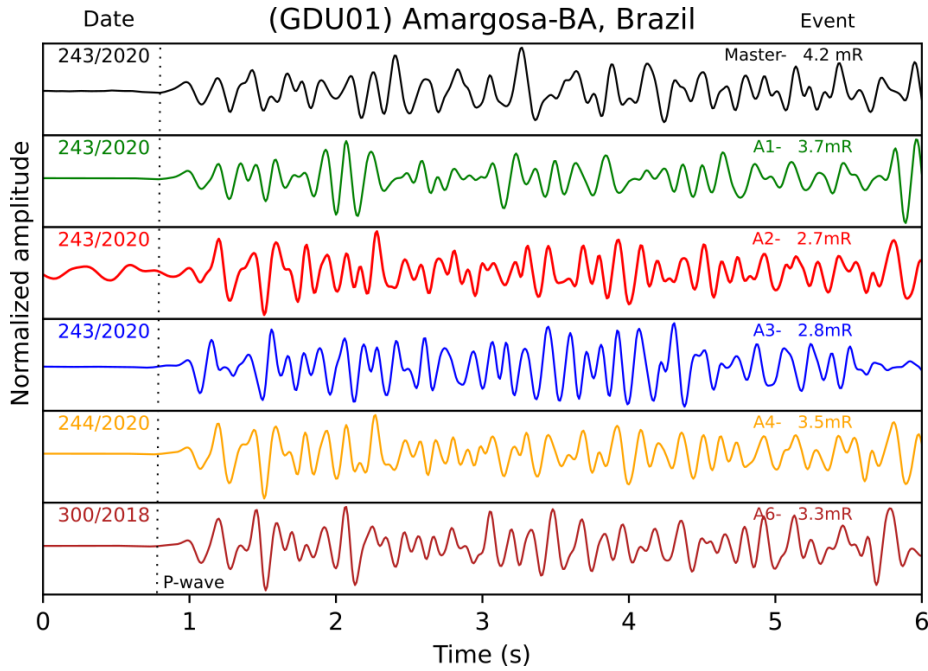
Figure 4.1: Waveforms of the mainshock and five aftershocks near Amargosa showing a noticeable similarity. ON.GDU01 station (79km), vertical component velocity records, band-pass filtered (2 - 8Hz). The event times (day of year/year) are displayed in the left corner, while the event number and magnitude are shown in the right corner. The dashed line indicates the P-wave arrivals.

Table 4.1 - Seismic events in Amargosa-BA region from 2018 to 2021. The M letter represents the main earthquake of the series, used as reference in the relocation. The numbers correspond the numbering assigned to each of these relocated events.

| N° evt	Origin	Longitude	Latitude	Magnitude (mR)
	2021-05-18 05:23:18	-39.57	-13.06	1.8
A4	2020-08-31 06:41:48	-39.58	-13.01	3.5
	2020-09-01 09:36:28	-39.59	-13.0	2.5
	2020-09-01 06:31:36	-39.60	-13.0	1.8
	2020-08-30 21:11:44	-39.57	-13.01	2.3
	2020-08-30 12:11:42	-39.60	-13.01	2.2
	2020-08-30 12:08:14	-39.60	-13.01	2.3
A3	2020-08-30 11:57:09	-39.61	-13.01	2.8
A2	2020-08-30 11:25:15	-39.60	-13.01	2.7
A1	2020-08-30 11:18:07	-39.58	-13.0	3.7
M	2020-08-30 10:44:28	-39.60	-13.01	4.2
	2020-08-30 10:43:43	-39.60	-13.0	2.5
A5	2019-11-09 07:30:24	-39.59	-13.01	3.3
A6	2018-10-27 06:36:57	-39.60	-12.98	3.3
	2018-10-24 21:34:22	-39.52	-13.04	2.2
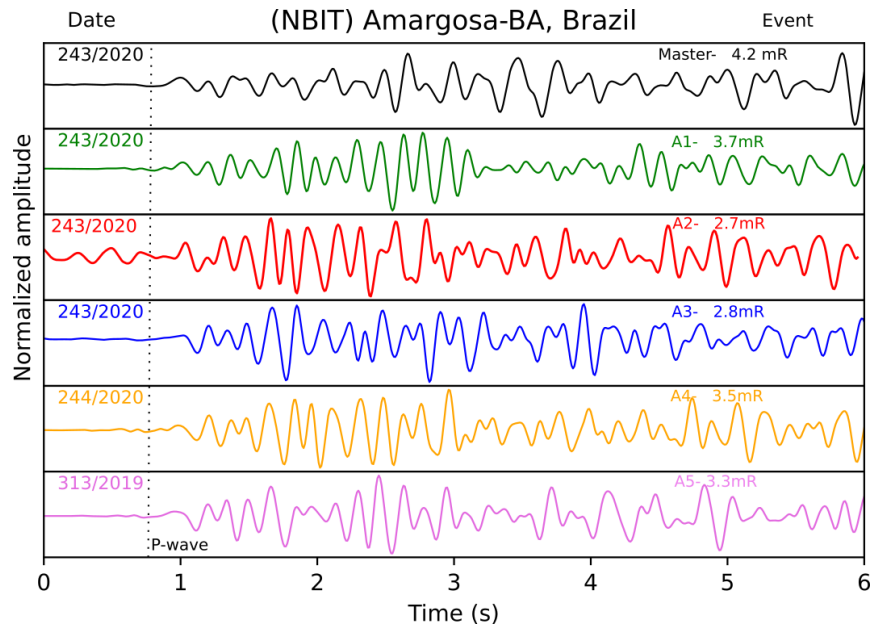
Figure 4.2: Waveforms of ON.NBIT station (214km), vertical component, velocity records band-pass filtered (2-8Hz).
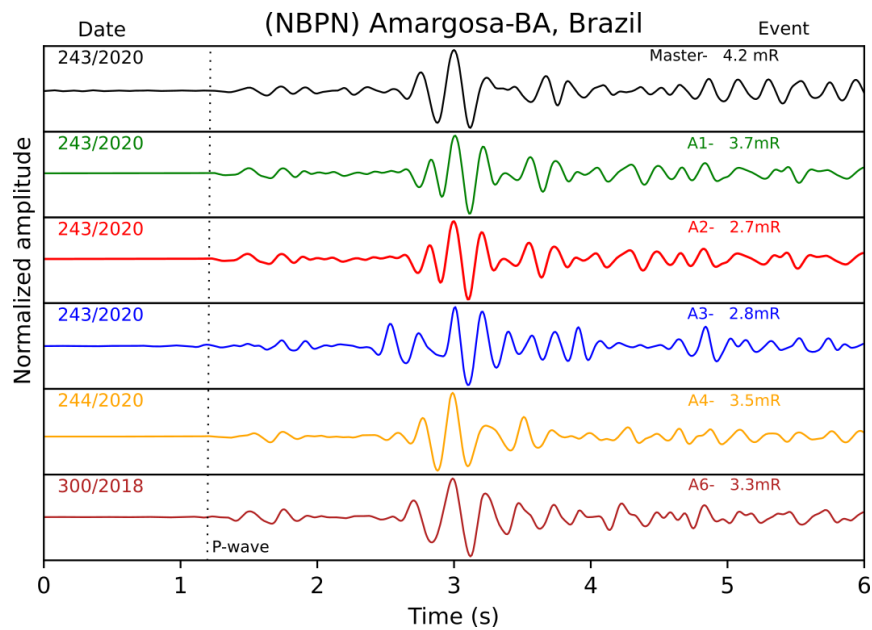

Figure 4.3: Waveforms of ON.NBPN station (248km), vertical component of recorded velocities, filtered with (2-8Hz) bandpass filter. Dashed line shows alignment by the Pn arrival.
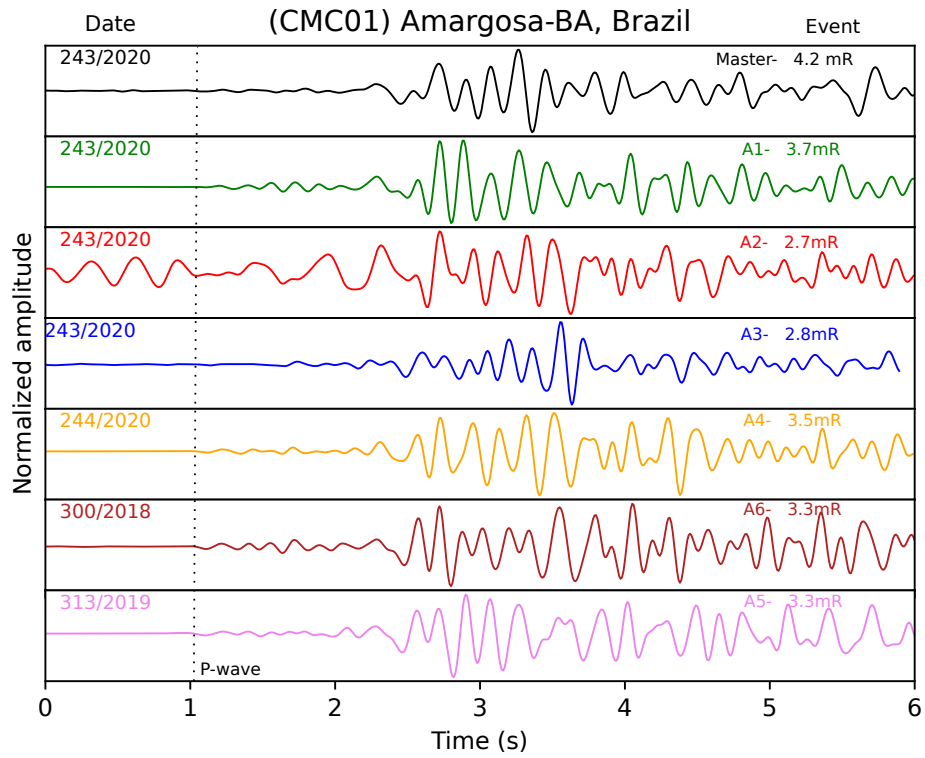
Figure 4.4: Waveforms of ON.CMC01 station (260km) depict the vertical component of recorded velocities, filtered with (2-8Hz) bandpass filter.
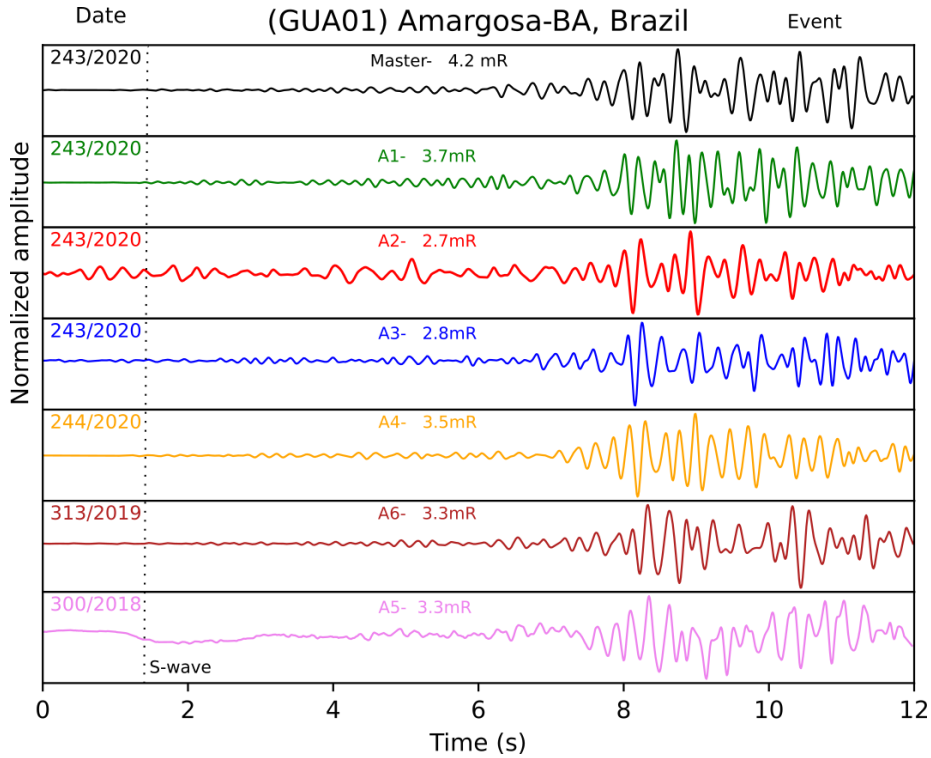
Figure 4.5: Waveforms of ON.GUA01 station (389km) depict the vertical component of recorded velocities, filtered with (2-8Hz) bandpass filter.

Using a local network installed after the mainshock, Fonsêca et al. (2021) found late aftershocks occurred at depths ranging from 0.5 to 1.5 km. In another study by Rivadeneyra-Vera et al. (2021), with a 3D velocity model developed for the South American Platform using RSBR stations, the Amargosa mainshock was located with an epicenter found to be 1.5 km away from the aftershock cloud observed by Fonsêca et al. (2021), and a depth of 5 km. Furthermore, through waveform modeling, Neto and Julià (2023) estimated a depth of 10 km for the event. Despite the differences, the three studies agree that the earthquakes have shallow depths.

Up until now, all the locations have been absolute **(Fig. 4.6)**, but this study aims to examine the source characteristics, and for this purpose, we will perform a relative location for some assigned larger events of the series (**Tab. 4.1**).
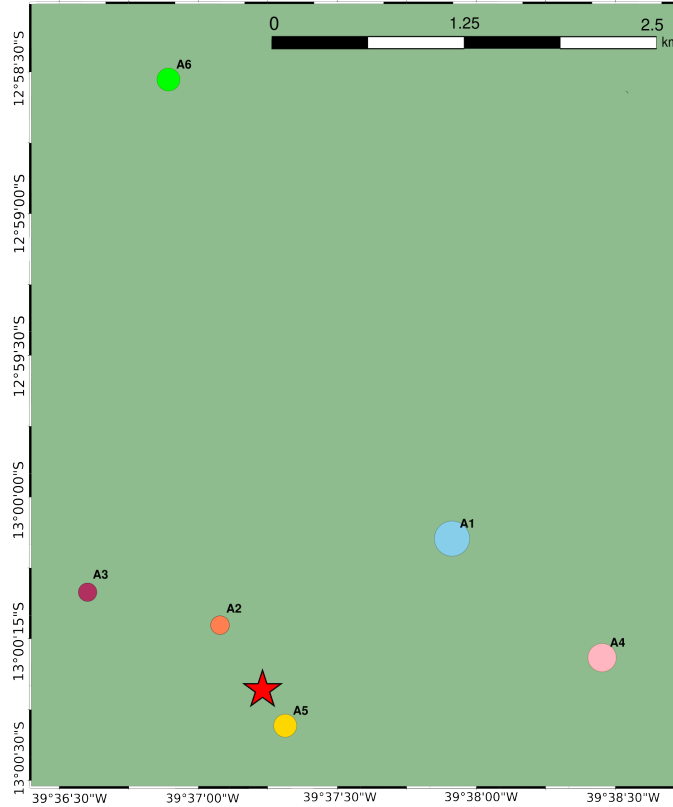
Figure 4.6: Absolute location made by USP seismological Center. We do not recognized any alignment, and the epicenter error can be up to 10 km for the smaller events.

4.1   Relative location

4.1.1   Sinusoidal time shift method

Using the matrix eq. (2.4) and the inversion procedure developed in this study (section 2.2), we relocated the larger earthquakes of the sequence, highlighted in **Tab. 4.1**, assuming a phase velocity of 3.3 km/s (a commonly used phase velocity for Rayleigh waves at approximately 1sec period, (e.g., Ciardelli and Assumpção (2019)) and adopting the mainshock of the series as a reference.

Fig. 4.7 shows the fit of the sinusoidal curve eq. (2.3) for these aftershocks. For all inversions, the RMS residual is less than 0.15s, the uncertainties of the parameters are well-behaved and the curve fits relatively well. The larger events have a greater amount of available data, however, a lack of stations with azimuths between 50°-150°, corresponding to the margin of the Atlantic Ocean, is evident for all events.
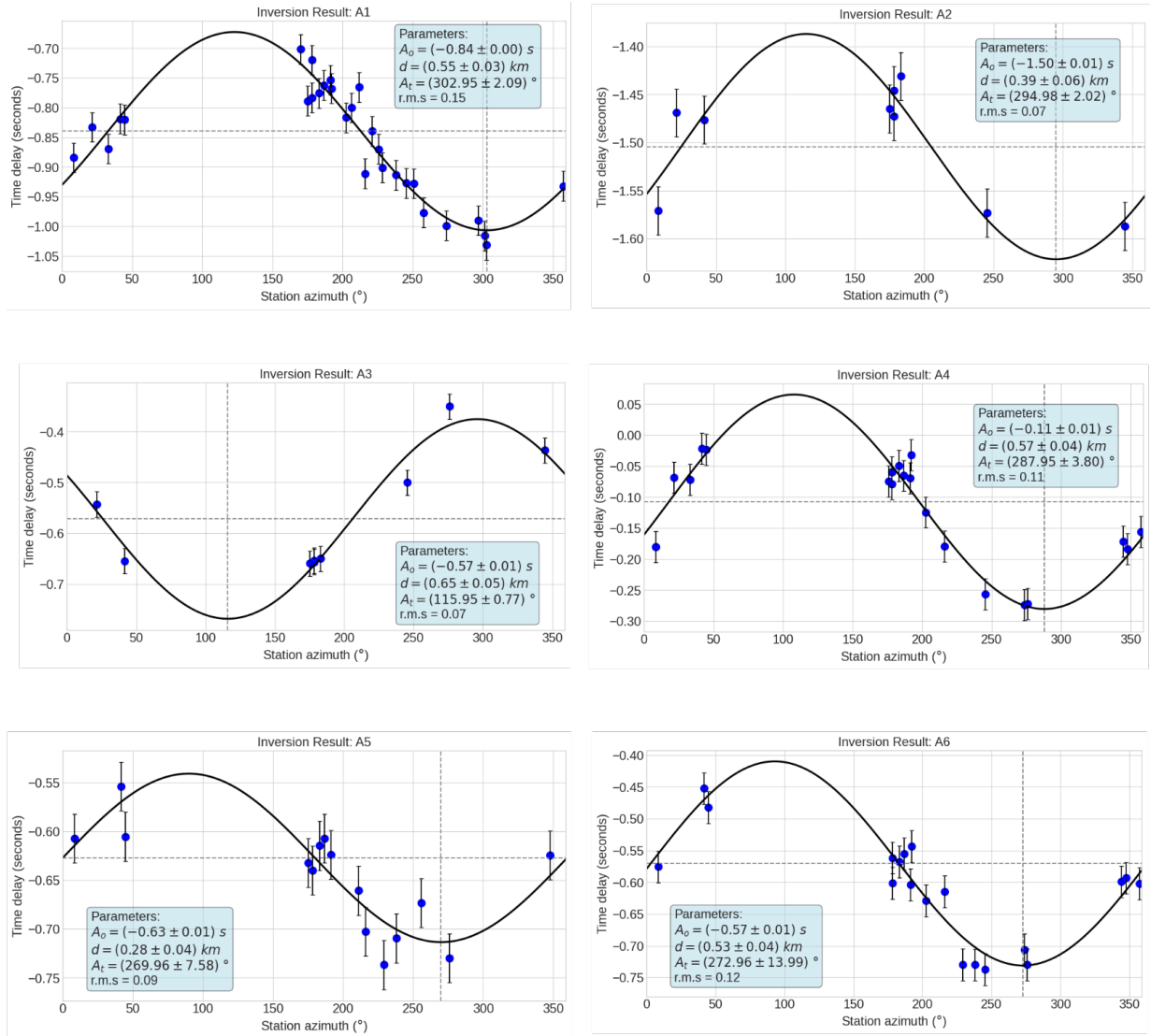
Figure 4.7: Fitted curve for the Lg relative location of the aftershocks. The solid line represents the best fit. The vertical axis represents the time delay (Tt-Tr) and the horizontal axis represents the azimuth (As). The blue points have a standard deviation $\sigma_o = 0.03s$. The light blue box displays the inverted parameters and their respective uncertainties. The vertical dashed line indicates the azimuth (At), while the horizontal dashed line indicates the time correction (Ao) of the target event relative to the reference.

After performing the relative location analysis, it was observed that all the aftershocks were located closer to the mainshock, within a distance of less than 700 meters, and displayed a WNW-ESE trend (**Fig. 4.8**).
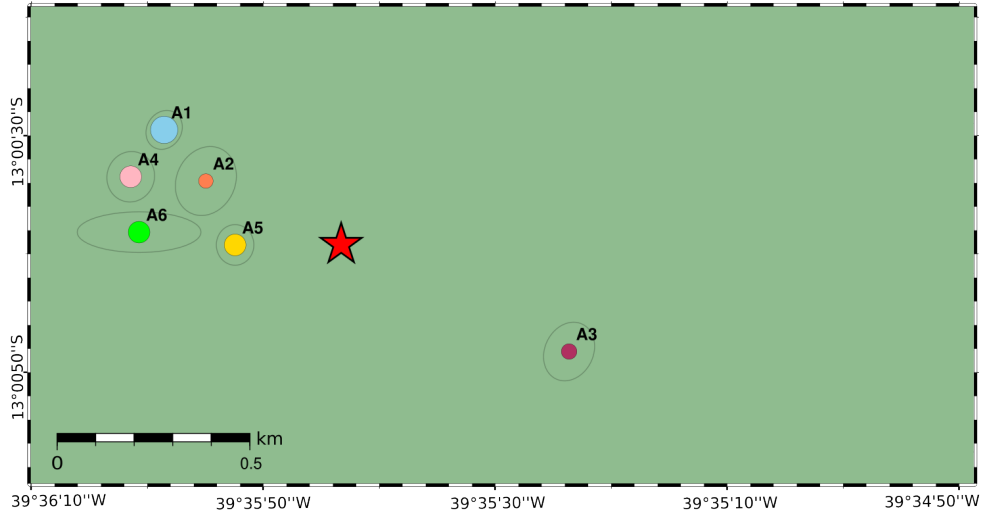
Figure 4.8: Location of Amargosa events. Red star is the reference (Master) event and circles the located target events using Lg waves only (eq. 2.3). This type of location has no depth determination.

4.1.1.1   Relative location with P-, S- and Lg-waves

In this section, we will incorporate the arrivals of both P- and S-waves to determine the relative positions of the aftershocks, as outlined in section (2.1). This will enable us to compare these results with the previous method. The key distinction lies in our ability to determine the depth of the events, which is essential for visualizing the fault plane where the aftershocks can possibly occur.

The relocated events, incorporating all phases (P-, S-, and Lg-waves), are depicted in **Fig. 4.9**. Now, with body waves information, we can generate a depth profile, along with the corresponding uncertainties, which suggests a subvertical dipping plane (**Fig. 4.10**). However, the uncertainties are too large to allow a good resolution for the dip of the rupture plane. However, On the other hand, with the data from the local network kindly provided by UFRN (Federal University of Rio Grande do Norte), we were able to plot a new depth profile with the late aftershocks, which resulted in a plane (96°, 22°) displayed in **Fig. 4.11**.

Figure 4.9: Location of Amargosa events. Red star is the reference (Master) event and circles the located target events using P-, S- and Lg-waves as described in section 2.1. The reference event has is depth fixed in 3km, this type of location can determine the depths of the target events.
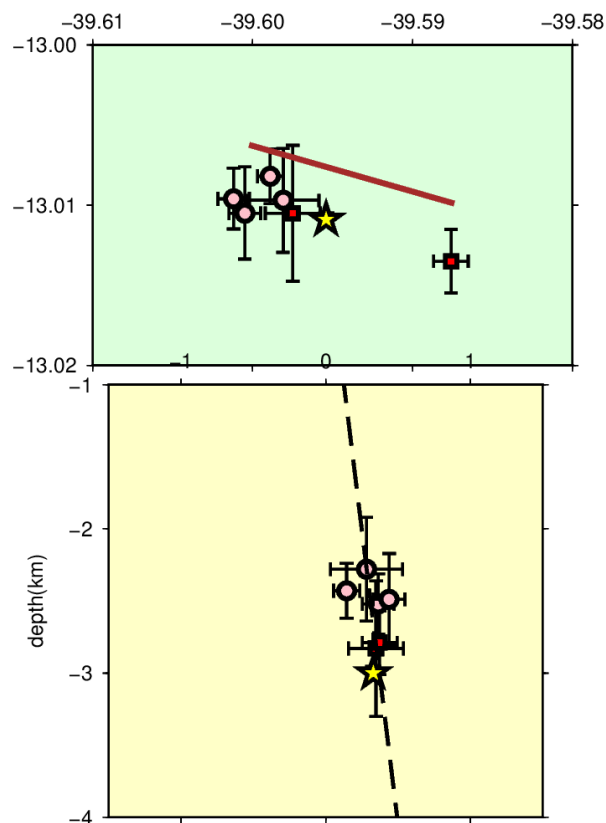
Figure 4.10: Aftershocks relocated through correlation of P-, S-wave and Lg-waves; pink circles are depths less than 2.5 km; red squares are depths more than 2.5km. Depth profile of the relocated events shows an almost vertically dipping plane (dipping to the SSE), but the large uncertainties do not allow a reliable determination of the plane dip.
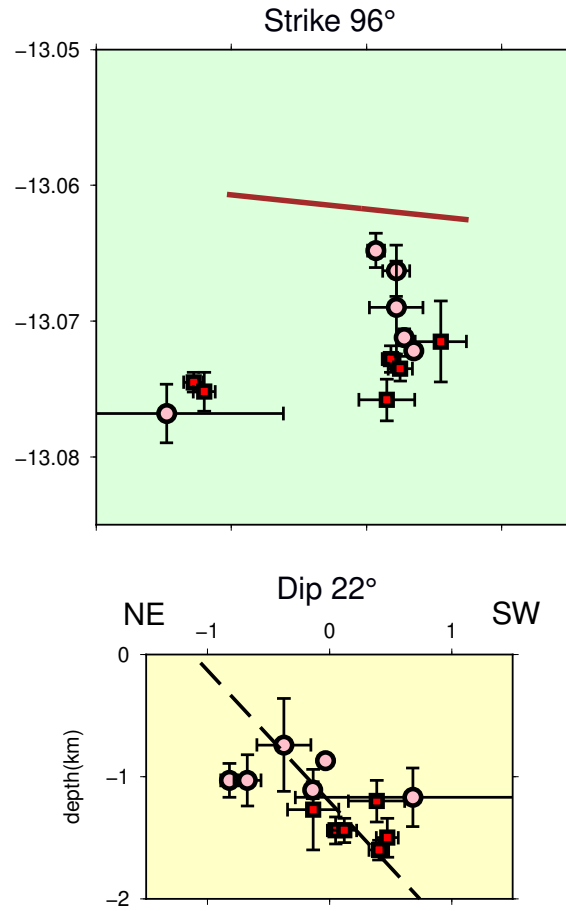
Figure 4.11: Late aftershocks depth profile by local UFRN stations. Striking 95° and dipping 22° to SW. Pink circles are depths less than 1.2 km; Red squares are depths more than 1.2km).

In the same way, **Fig.** **4.12** and **4.13** show relative locations produced only by body and Lg-waves respectively. Regardless of the method used and the phases included, the aftershocks still aligned in the WNW-ESE direction, with an estimated length of approximately 1200m (distance from A1 to A3 events).

Upon analyzing the location results, we can conclude that the four independent determinations exhibit a high level of agreement, with an average error of approximately 100m relative to one another. The relatively larger error in longitude can be attributed to the absence of east-west stations for P- and S-waves. Nevertheless, by incorporating Lg-waves, we are able to utilize more distant stations, leading to a significantly improved azimuthal coverage and enhanced accuracy in constraining the longitude. Additionally, referring to the previous absolute location results (**Fig.** **4.6**), it was found that the aftershock A6 had the highest displacement, moving approximately 4 km in the Master event direction. A5 and A6 events showed a discrepancy in their body-wave locations, and the reasons for this

are still uncertain. However, even if hypothetically they are outside the 2020 fault zone (as P and S-wave data seems to suggest), we still observe a WNW-ESE trend and a length of 1200m.
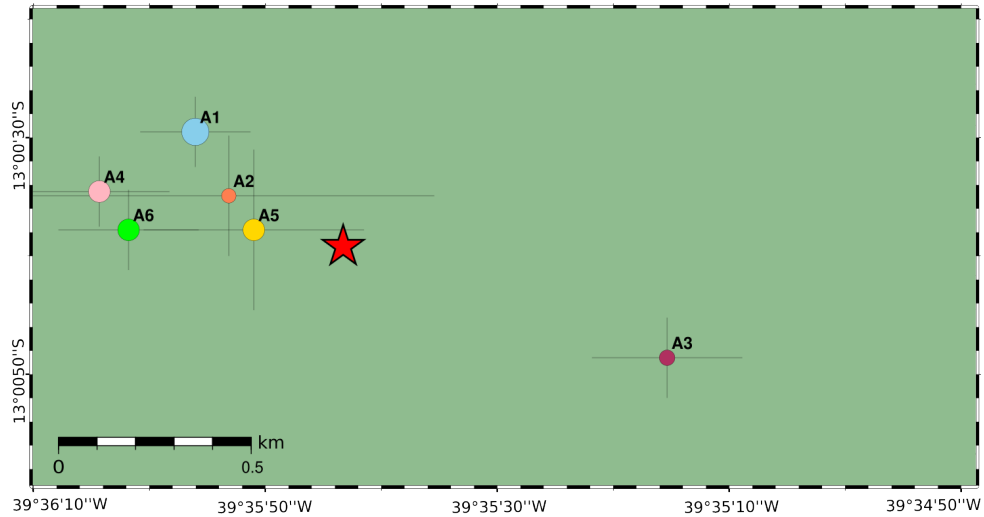

Figure 4.12: Location of Amargosa events. Red star is the reference (Master) event and circles the located target events using only P- and S-waves. this type of location can determine the depths of the target events. The errors are larger due to the limited number of station, especially in the longitudinal direction. A5 and A6 epicenter are outside of the map.

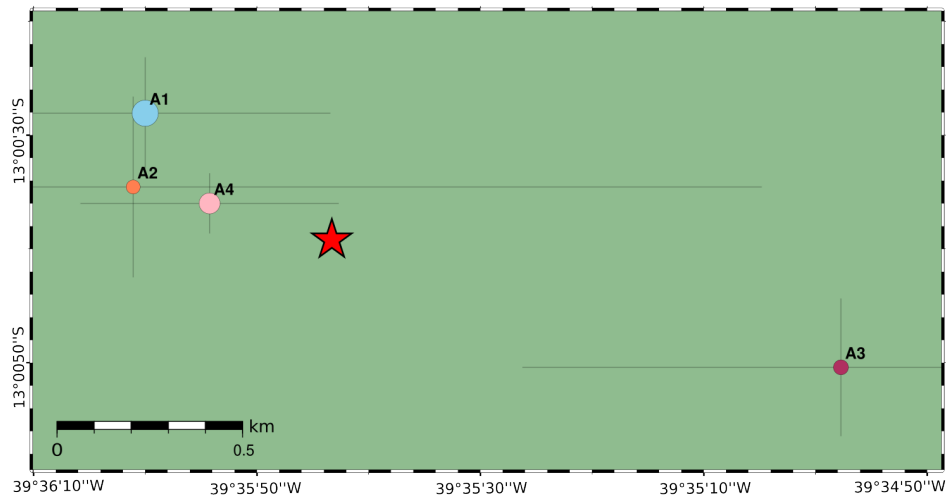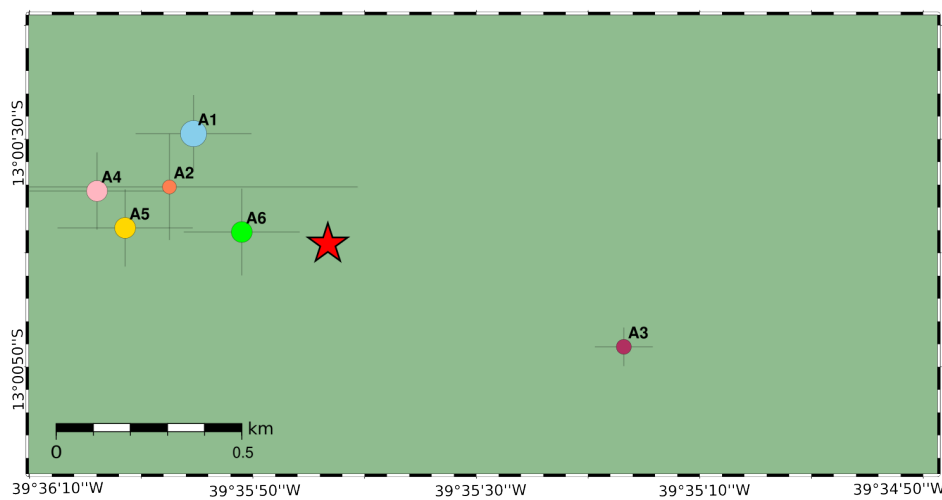*Figure 4.13:* Location of Amargosa events. Red star is the reference (Master) event and circles the located target events using only Lg-waves. This type of location has no depth determination.

4.2   *Focal mechanism by waveform inversion*

In support to the relocation analysis, we determined the focal mechanism for the main event of the series. Integrating this additional analysis into our study, aims to provide further validation and match with the results obtained through the relative location method and make valuable insights into the source orientation and characteristics of the faulting involved in the seismic activity.

The FMNEAR software (Delouis, 2014) was employed to determine the focal mechanism in our study. This method utilizes waveform inversion to determine the focal mechanism of the mainshock.

To model the waveform, we chose a band-pass filter (0.04-0.1 Hz) to reduce the effects of small-scale crustal heterogeneities. A 10-layer velocity model, as described in **Tab. 4.2**, was utilized. For the inversion, we considered only stations at less than 5°. P-wave arrivals were visually picked and used by the FMNEAR code to correlate the synthetics with the observed traces.

Table 4.2 - A ten-layer model including velocity, density and attenuation used for waveform modeling. Model based on Rayleigh-wave dispersion curves (Shirzad, personnal communication).

Layer	Thickness (km)	Vp (km/s)	Vs(km/s)	Density(g/cm^3)	Qp	Qs
Crust 1	1.00	5.980	3.470	2.690	500	250
Crust 2	2.00	6.183	3.592	2.755	500	250
Crust 3	3.00	6.320	3.675	2.798	500	250
Crust 4	4.00	6.360	3.690	2.810	500	250
Crust 5	6.00	6.410	3.725	2.822	500	250
Crust 6	5.00	6.700	3.880	2.870	500	250
Crust 7	5.00	6.800	3.950	2.930	500	250
Crust 8	14.0	6.900	4.030	2.970	500	250
Crust 9	25.0	7.930	4.600	3.290	500	250
Mantle	00.0	7.989	4.640	3.306	500	250

Fig. 4.14 shows the modeled waveforms and a thrust fault solution (135°, 40°, 101°), with NNE-SSE compressional-axis by inverting six regional stations. The N-S component (NS at station NBIT, was not operating properly and could not be fitted. Component E and Z in NBLA station, did not match well with the real seismogram. In some cases, the synthetic waveform amplitude is slightly overestimated, like in CMC01 and NBPN (N and E components).
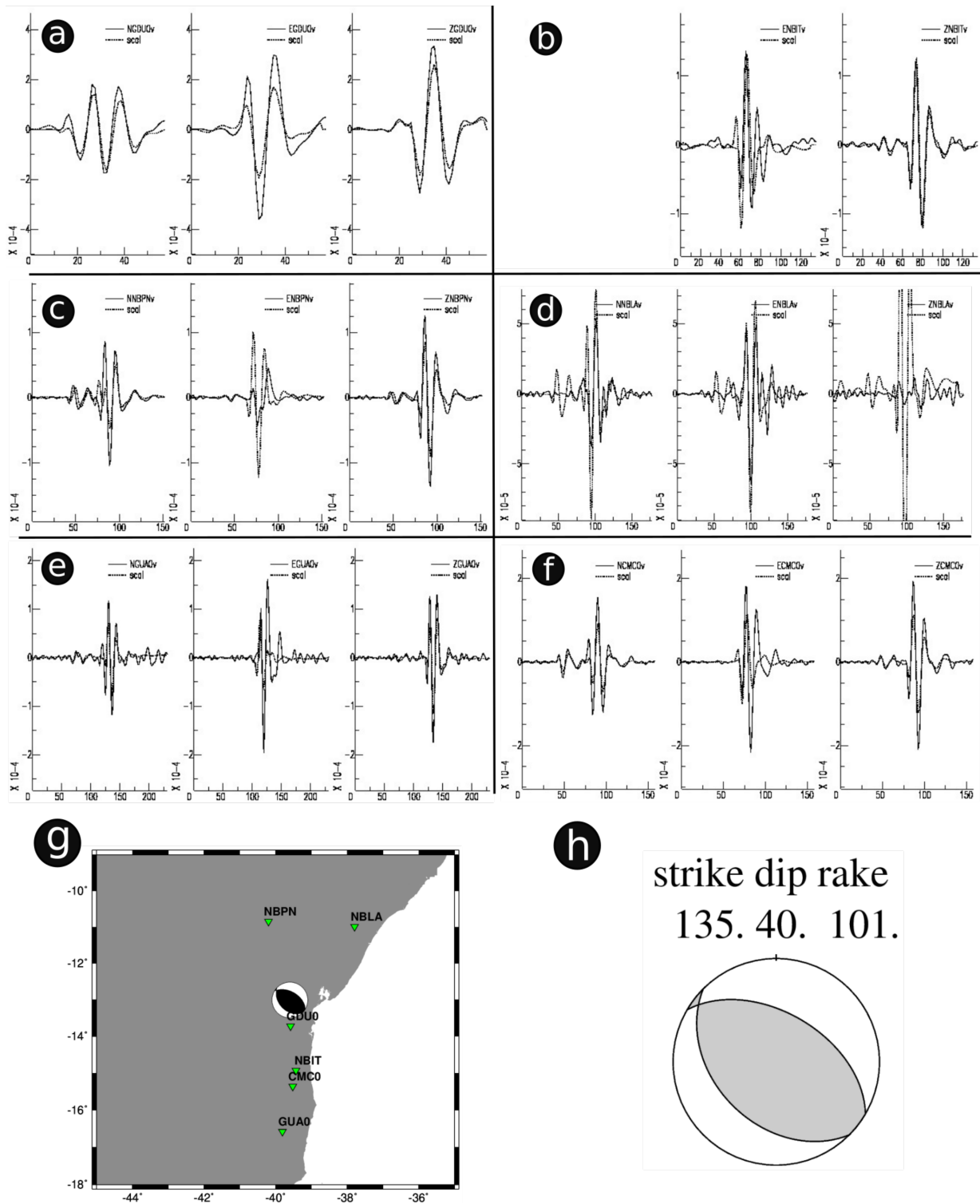
Figure 4.14: Modeling results for the Amargosa earthquake for the three components, station map, and focal mechanism result. The numbers in the figure are: (a) Station GDU01; (b) Station NBIT (North component was not working); (c) Station NBPN; (d) Station NBLA; (e) Station GUA01; (f) Station CMC01; (g) Epicenter and locations of the 6 stations utilized in this study; (h) Focal mechanism result. All waveforms are filtered at 0.04-0.1 Hz. Solid black traces denote observations while dotted black traces denote predictions.

In addition to waveform inversion, we incorporated analysis of 24 P-wave polarities and performed a refinement of the fault planes. The combination of waveform inversion and polarity analysis (**Fig. 4.15**) provided a more robust and accurate characterization of the source mechanism. Polarities symbols on focal sphere were scaled by quality, larger symbols denote clear, reliable polarities. In order to fit the waveform inversion result to the P-wave polarities, we slightly rotated the waveform inversion result to the adopted solution (120° , 50°, 120°).
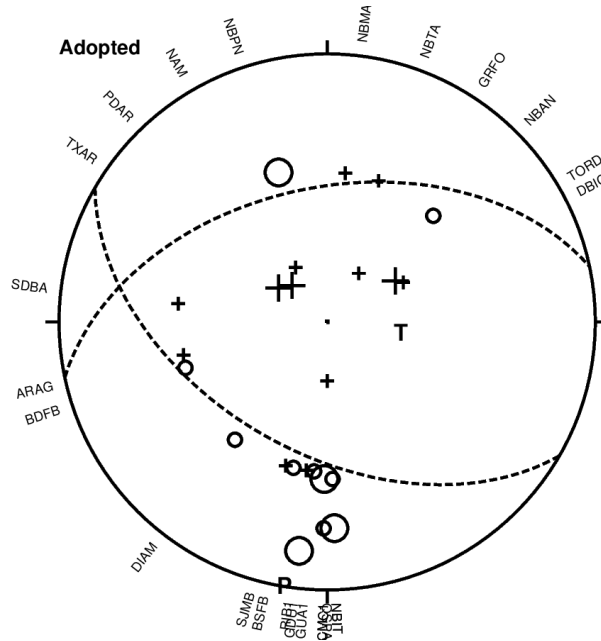
Figure 4.15: Adjustment of the FMNEAR solution to the first-motion P-wave polarities. Crosses represent compression, circles dilation. The size of the symbols corresponds to the quality of the data. Station are plotted according to the azimuthal angle. All high-quality data are in agreement with the adopted fault plane solution (120°, 50°, 120°).

Most polarities (19 out of 24) agree with our adopted mechanism. The conflicting data is of low-quality and is close to the nodal planes, which makes it more difficult to read the polarity due to the low amplitude of the waves. All high-quality observations are in agreement with the adopted nodal plane solution. The preferred depth of 1km for the waveform inversion matches well with the findings of Fonsêca et al. (2021) in their local network study, where they reported aftershock depths ranging from 0.5 to 1.5 km. Importantly, the adopted focal mechanism (**Fig. 4.15**) agrees with WNW-ESE aftershock alignment, which reinforces the validity of the relocation method. Despite this, the subvertical dipping plane indicated by the relocated events (**Fig. 4.10**) does not

coincide with the dips of the fault planes of the focal mechanism. This discrepancy arises from the large depth uncertainties in the relocated hypocenters, as reflected by the large vertical error bars. However, when analyzing the depth profile based on UFRN local data (**Fig. 4.11**), we found a dipping plane (22°) towards the southwest, which is more consistent with the 50° dip of the adopted focal mechanism.

Clearly, the normal fault solution and the 10km depth of Neto and Julià (2023) are not compatible with our solution and the preliminary results of the local network (Fonsêca et al., 2021). It may be that the "Cut And Paste" method used by Neto and Julià (2023) with distant regional stations is not appropriate for this relatively small magnitude event.

4.2.1 Stress drop estimative

According to the distribution of aftershocks calculated here, we can assume a rupture length (L) of 1200m. We estimated the stress drop for the Amargosa mainshock using the seismic moment (M_o) and a circular fault rupture with radius r (= half the rupture length = L/2), following the theoretical equation for a circular fault model of Brune (1970, 1971):

$$\Delta\sigma = \frac{7}{16}\frac{M_o}{r^3} \tag{4.1}$$

First, to calculate the seismic moment M_o, we use the Hanks and Kanamori (1979) relationship $M_w = (\log_{10} M_o - 9.5)/1.5$, obtaining a value $M_o = 1.53.10^{15}$ based on $M_w = 4.09$ as determined from waveform inversion. The estimated stress drop for a total fault length L = 1200m and Mw = 4.09 is approximately 3.1 MPa.

This value is consistent with the results reported by Ciardelli and Assumpção (2019), which indicated that stress drops in Brazil commonly lie within the range of 0.1 to 10 MPa. These values are lower than the average Brune stress drop of 10 MPa indicated by the empirical studies of Wells and Coppersmith (1994).

4.2.2 Discussion and tectonic settings

The Amargosa region is located on the boundary between the Jequié Block, with an age of approximately 2.8 billion years, and the Itabuna-Salvador-Curaçá Belt, with an age of approximately 2.6 billion years. These geological formations are part of the crystalline basement of the São Francisco Craton and mainly consist of granulitic rocks (Barbosa and

Sabaté, 2002, 2004). These rocks form the crystalline basement of the Phanerozoic deposits in the area, which are largely associated with the breakup of Pangaea supercontinent. The Phanerozoic basins in the region are characterized by NNE-SSW oriented faults with WNW-ESE transfer structures. One of these transfer structures is the Salvador Shear Zone (SSZ), which crosses the city of Amargosa. **Fig. 4.16** shows a regional map of the deformational structures in the proximal and distal regions of these basins (Ferreira et al., 2009).
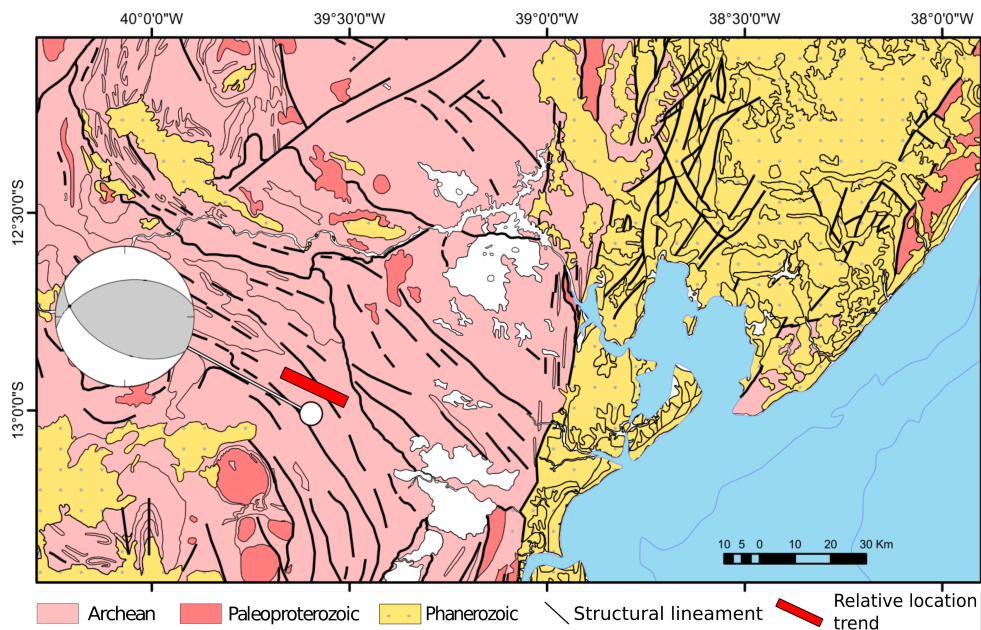

Figure 4.16: Simplified geotectonic and structural map of the region of Amargosa-BA. The adopted focal mechanism and relocation trend are plotted in the map. The NW-SE lineaments near the epicenter (white circle) represent the Salvador Shear Zone (SSZ). Lithology and structural data from the Brazilian Geologic Survey (CPRM).

The available data suggests the possibility of reactivation of pre-existing NW-SE-oriented shear structures, which align with both, the relative location and one of the nodal planes of the focal mechanism. However, without a detailed mapping of the fault region, we cannot definitively state that the Amargosa events are nucleated on these pre-existing structures.

The NNE-SSW orientation of the P axes of our preferred focal mechanism is not consistent with the average E-W maximum horizontal compression observed in Minas Gerais (Assumpção et al., 2016). However, P axes aligned roughly parallel to the continental coast is a common feature in intraplate stress field, and are due to local effects from lateral

density contrasts between continental and oceanic crust (**Fig. 4.17**), as well as due to local flexural stresses from sediment load in the continental shelf (e.g., Assumpção et al. (2016)). In fact, breakout data from oil wells in Bahia show an average SHmax parallel to the coastline (Lima et al., 1997).

SHmax from Focal Mechanisms
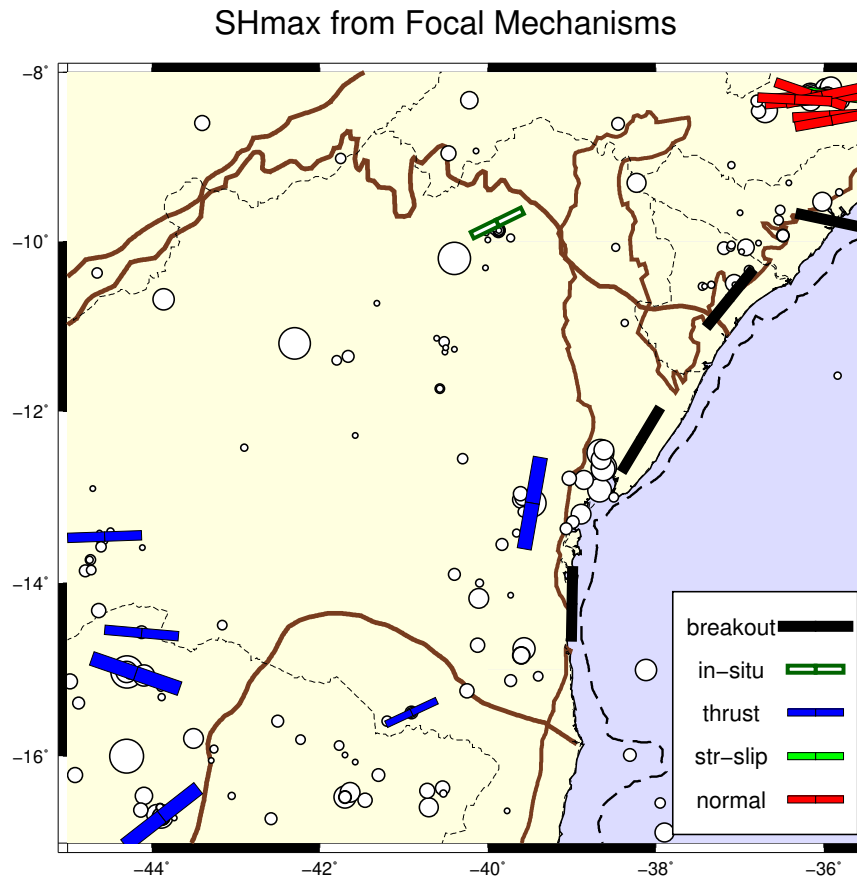
Figure 4.17: Data from maximal horizontal stress orientations (SHmax). Bar size indicates data quality. White circles denote earthquakes. Major geological provinces are São Francisco Craton and Recôncavo-Tucano-Jatobá basin.

Chapter 5

Sete Lagoas sequence

From March to December 2022, a series of earthquakes took place in close proximity to the city of Sete Lagoas (MG). These seismic events were widely felt across the city, with a notable impact in the southern neighborhoods. The "Sentiu Aí?" platform, operated by the Center for Seismology at USP, received a significant number of reports originating from this specific area. Activity in the area is known since at least 2016. A total of 14 events were recorded during this period, with the largest one reaching a magnitude of mR 2.9 (**Tab. 5.1**). Particularly, this seismic event appears to be associated with open-pit mining activities in the area, which may cause local stress imbalance due to the extensive extraction of limestone.

Table 5.1 - Major earthquakes of Sete Lagoas-MG. All events in the table are relocated in this study. Letter M (Master) indicates the reference event. The event numbers were assigned to each of these relocated events. The coordinates were taken from the Brazilian Seismic Bulletin and are absolute locations.

N° evt	Date - hour	Longitude	Latitude	Magnitude (mR)
S13	2022-12-28 - 03:42:30	-44.22	-19.51	2.9
S12	2022-11-24 - 02:02:35	-44.17	-19.52	2.2
S11	2022-07-29 - 20:44:51	-44.24	-19.50	2.9
S10	2022-07-25 - 14:56:05	-44.25	-19.49	2.2
S9	2022-06-27 - 08:16:38	-44.23	-19.50	2.5
	2022-06-27 - 01:08:19	-44.25	-19.49	2.0
S8	2022-06-06 - 13:49:11	-44.22	-19.50	2.0
S7	2022-06-01 - 03:17:34	-44.20	-19.51	2.2
S6	2022-05-31 - 00:38:58	-44.25	-19.45	2.2
S5	2022-05-30 - 15:01:47	-44.26	-19.48	2.1
	2022-05-30 - 13:58:47	-44.26	-19.45	2.1
S4	2022-05-29 - 20:33:42	-44.26	-19.48	2.2
S3	2022-05-20 - 22:36:31	-44.26	-19.50	2.7
S2	2022-05-16 - 02:17:37	-44.25	-19.50	2.1
S1	2022-05-08 - 10:48:59	-44.28	-19.49	2.0
M	2022-04-30 - 00:53:17	-44.25	-19.50	2.9

Fig. 5.1, 5.2 and 5.3 show waveforms from several aftershocks recorded by regional stations. Additional S-waves correlation figures from Sete Lagoas can be found in the **Appendix** B.
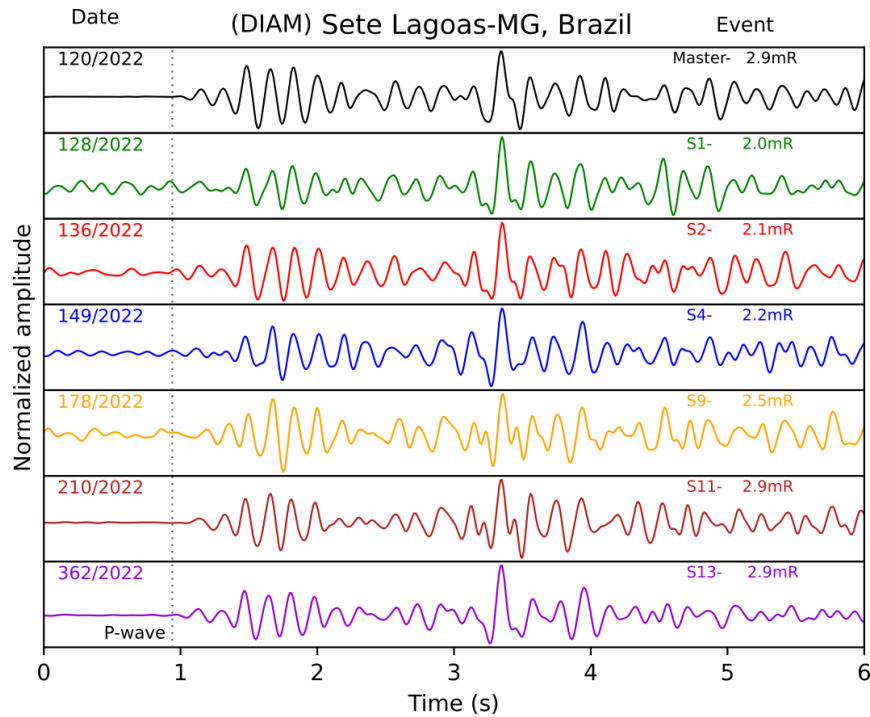
Figure 5.1: Waveforms of the mainshock and six aftershocks near Sete Lagoas, showing a very high similarities on BL.DIAM (142km). P waves, vertical component velocity records, band-pass filtered (2-8Hz). The event times (day of year/year) are displayed in the left corner, while the event number and magnitude are shown in the right corner. The dashed line indicates the P-wave arrivals.
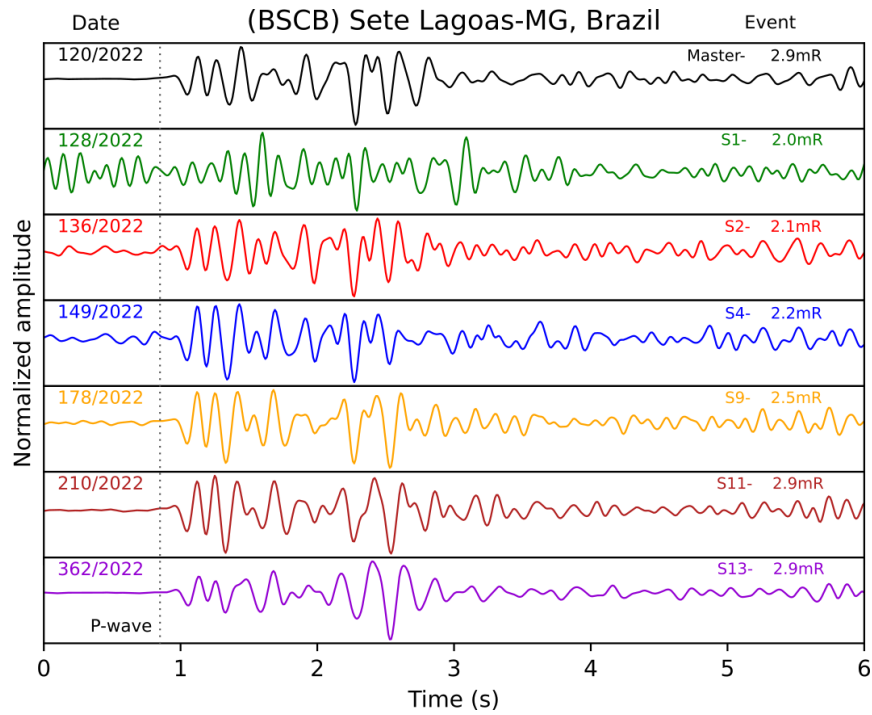
Figure 5.2: Waveforms of BL.BSCB station (174km), P-waves, vertical component, velocity records band-pass filtered (2-8Hz).
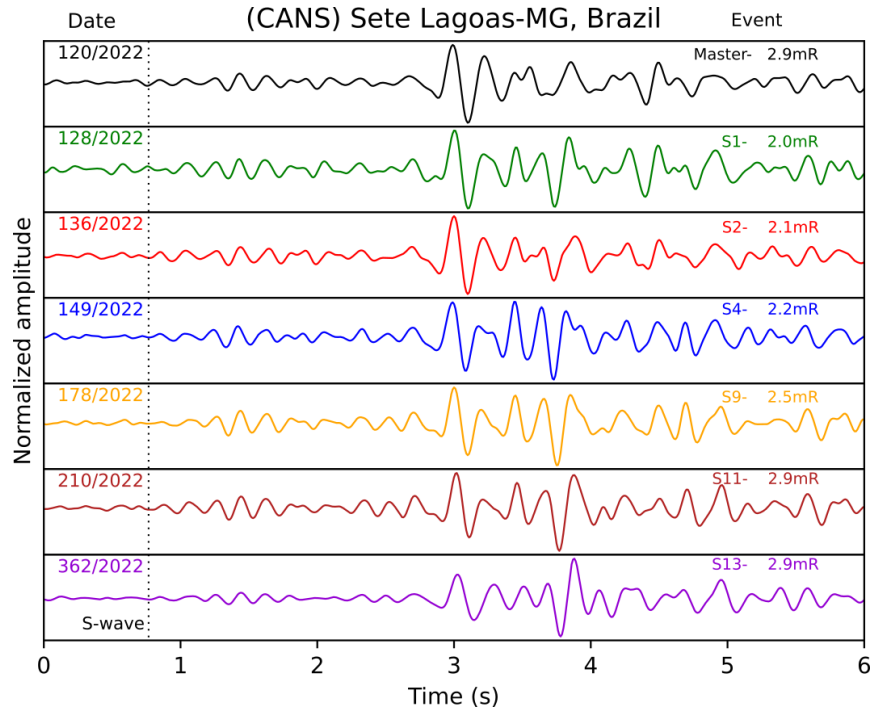

Figure 5.3: Waveforms of BL.CANS station (240km), vertical component, velocity records band-pass filtered (2-8Hz). For this station, the dotted line represents the arrival of S-waves.

The absolute locations (**Fig. 5.4**) show a scattered distribution, especially with earth-

quakes of low magnitude 2.0-2.2 mR as they have a low SNR ratio. For these small earthquakes, the location is made using only 3 or 4 stations, which significantly emphasizes the importance of relative relocation to better understand the spatial distribution of events over time that has been occurring regularly since early 2022.
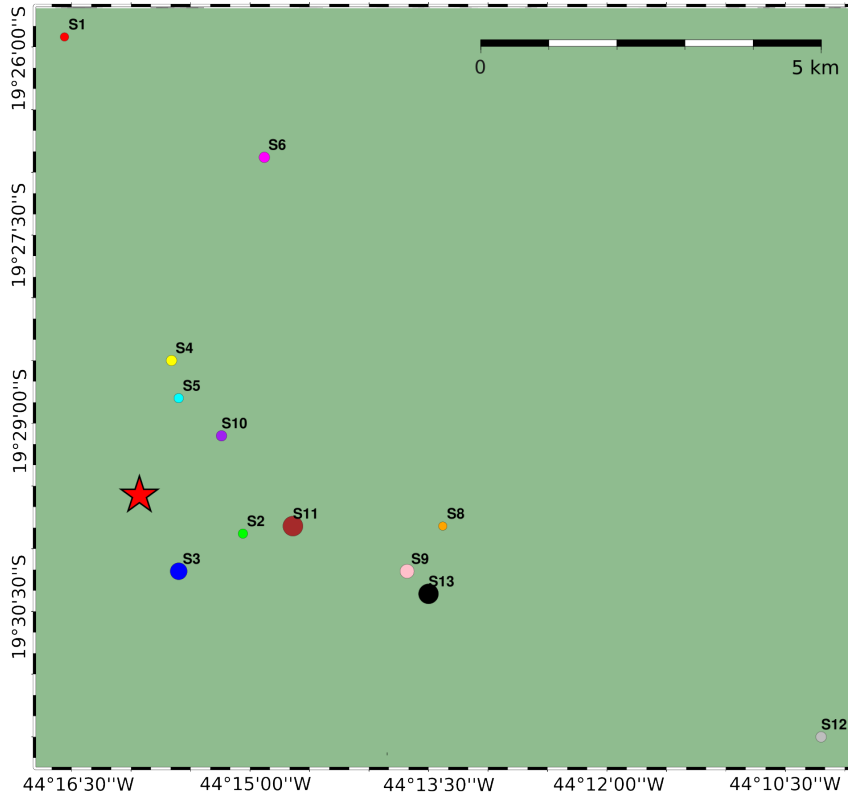

Figure 5.4: Absolute location by USP Seismological Center using regional stations. The aftershocks exhibit a sparse distribution (colored circles), located approximately 1km or more away from the main event (red star).

5.1 Relative location

5.1.1 Rayleigh time shift method

From matrix Eq. (2), we relocated the numbered events in **Tab.** **5.1** by using an Lg-wave phase velocity of 3.1 km/s, as inferred from the regional velocity model by Shirzad et al. (2022). The 30/04/2022 event was chosen as the reference. **Fig.** **5.5** and **5.6** compile the thirteen inversion results.
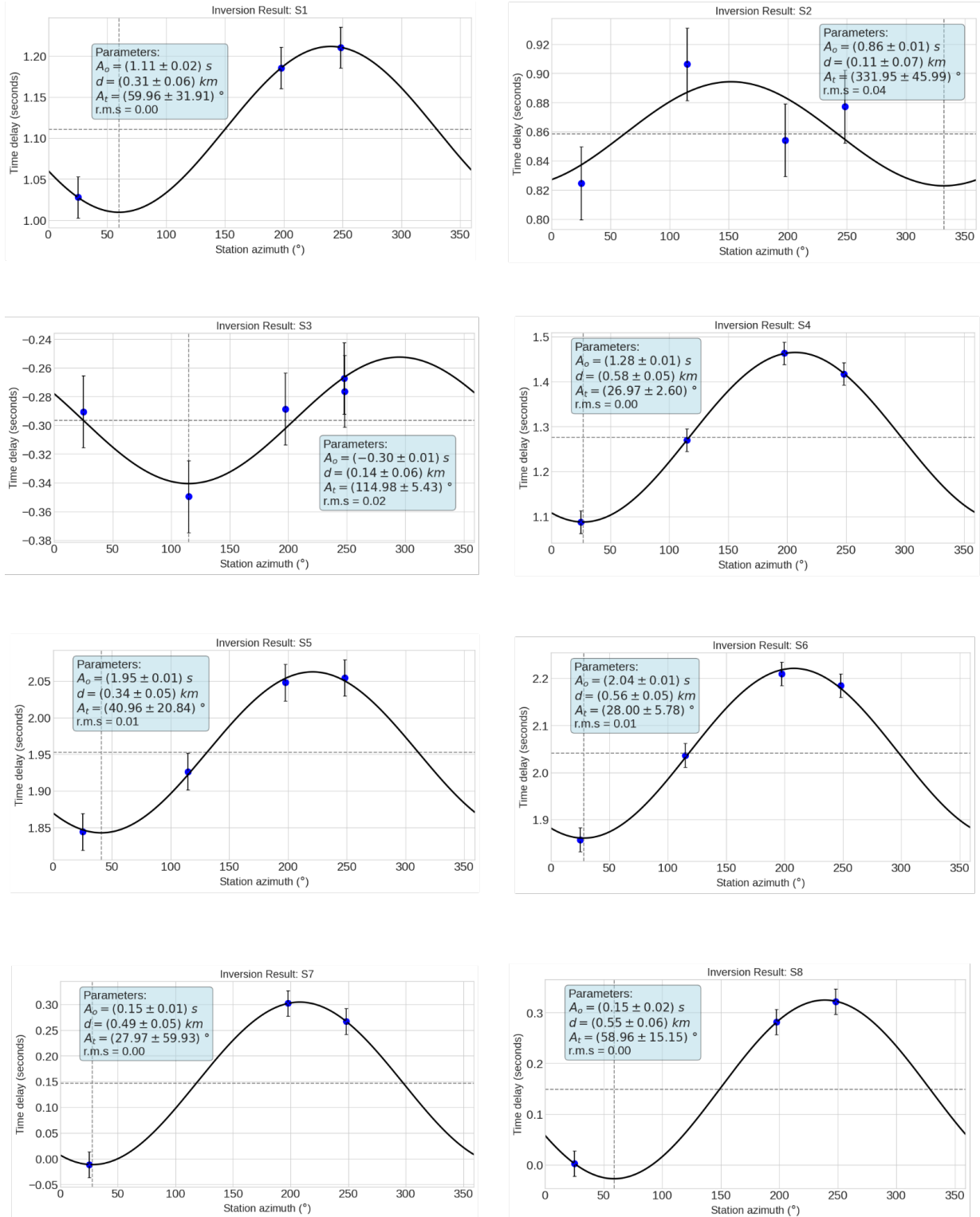
Figure 5.5: Fitted curve for the Lg relative location of the aftershocks (S1-S8). The solid line represents the best fit, and the blue points represent the time shift measurements with their associated error $\sigma_o = 0.03s$. The vertical axis represents the time delay $(T_t - T_r)$ and the horizontal axis represents the azimuth (A_s). The light blue box displays the inverted parameters and their respective uncertainties. The vertical and horizontal dashed line indicates the azimuth (A_t) and the time correction (A_o) of the target event relative to the reference, respectively.
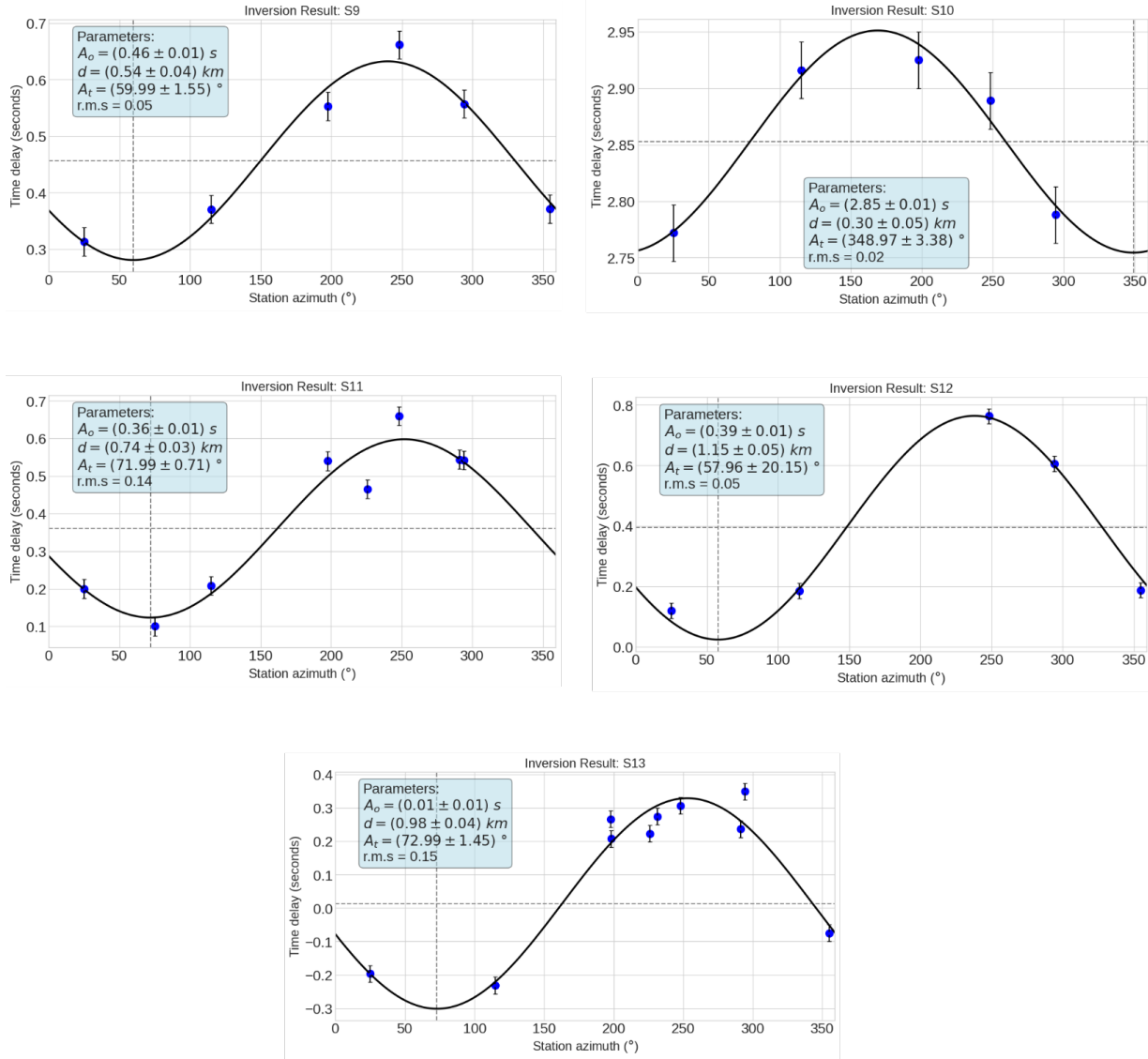
Figure 5.6: Fitted curve for the Lg relative location of the aftershocks (S9-S13).

For some curves, we only have 3 observations, due to low-magnitudes (2.0-2.2 mR). However, the waveform correlations are clear, and we have an acceptable azimuthal coverage. For all events, the RMS residual is < 0.15s. Overall, the curve fits relatively well and the parameter uncertainties are well-behaved, despite some large errors in At (relative azimuth) of S1, S2, S7 and S12 events. Here, we remind that the At parameter was excluded from the parameter vector eq. (2.4), and the uncertainty calculations (section 2.2.1) were independently estimated through uncertainty propagation with eq. (2.6). This method does not seem to provide reasonable values when we have few measurements. In general, with few data points available, the curve-fitting process becomes more susceptible to noise,

outliers, and inaccuracies. Based on that observations, we attest that this method is not good at estimating the uncertainties of the parameter A_t when we have few measurements, given that some values in a small data set can have a significant impact on the calculations. However, besides these four events, the method provides reasonable errors.

Fig. 5.7 displays the relative location results obtained through Lg time shift measurements. **Fig. 5.8**, **5.9**, and **5.10** present the relative locations related to: P-, S-, and Lg-phases; P and S phases; and only Lg-waves, respectively, all using the HYPOSAT code (Schweitzer, 2001). It is important to note that the last three figures are the result of the station correction method discussed in section 2.1 and should not be mixed up. Comparison of the resulting patterns from different methods and datasets, helps to provide a better assessment of the robustness of the relative locations.
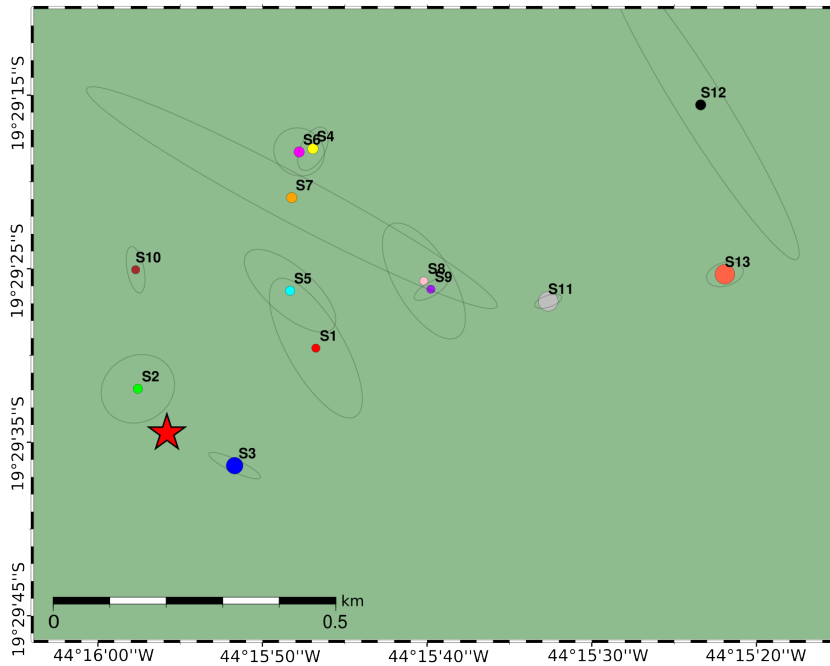
Figure 5.7: Relative location of Sete Lagoas events using the Lg waves (eq. 2.1). Red star is the reference (Master) event and circles the located target (eq. 2.1). This type of location has no depth determination. Take note on large error ellipses resulting from the parameter At estimation for the events S1, S2, S7 and S12.

In general, all locations show consistency among themselves. The more noticeable discrepancies (differences between different methods) was observed for the solo P- and S-wave relocation, notably for events S3 (350m), S5 (230m) and S12 (420m). These discrepancies occur because body wave phases are highly dependent on an accurate velocity model and precision in the pick times (due to the high velocity propagation). For all the other events
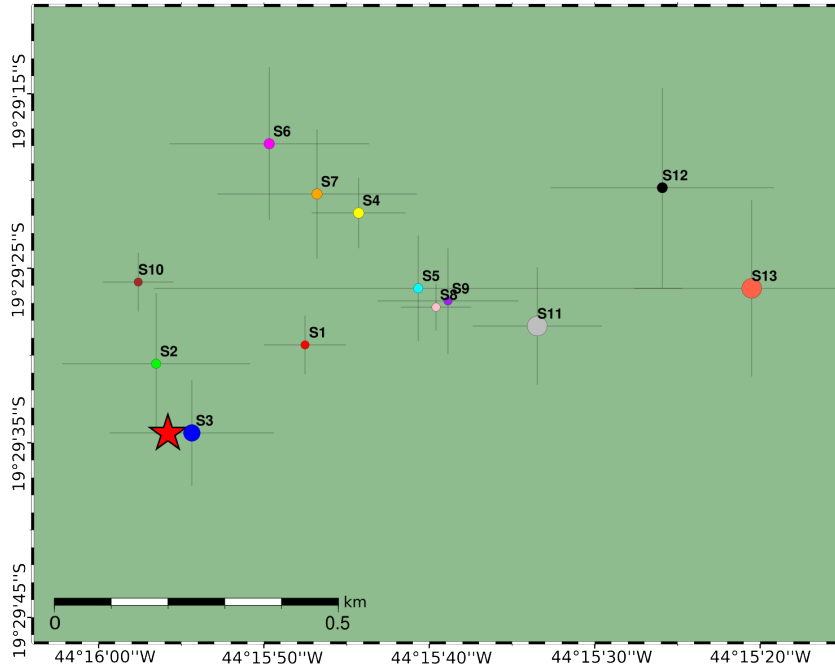
Figure 5.8: Location of Sete Lagoas events. Red star is the reference (Master) event and circles the located target events using P-, S- and Lg-waves. The reference event has its depth fixed at 1km, this type of location can determine the depths of the target events.

and location procedures, the differences are less than 150 meters. This good correlation allows us to discuss the overall relocation results. Given that, we will work with two hypothesis:

first hypothesis:

Contrary to the Amargosa sequence, no obvious trend is observed here. The aftershocks are predominantly located to the northeast of the main event within a range of 100 to 1100 meters, resembling a cloud or earthquake swarm. It is possible that they represent multiple independent fault ruptures with a similar focal mechanism.

Another observation in **Fig. 5.7** ,**5.8**, **5.9**, and **5.10** is that the early aftershocks, such as 08/05 (S1), 16/05 (S2), and 20/05 (S3), are located near the mainshock, while late aftershocks, such as 29/07 (S11), 24/11 (S12), and 28/12 (S13), are located further away from the main event. This pattern suggests a possible epicentral migration, indicating the potential lateral propagation of the fault rupture. This phenomenon aligns with the mechanical theory of stress increase at the fault edges, as described by Das and Henry (2003).
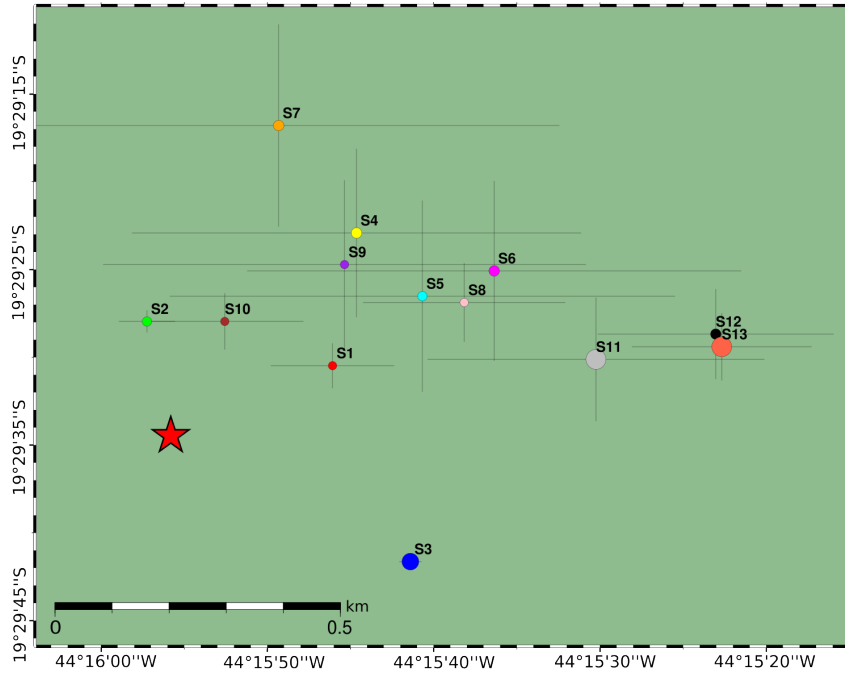
Figure 5.9: Location of Sete Lagoas events. Red star is the reference (Master) event and circles the located target events using only P- and S-waves. The errors are larger due to the limited number of stations. Events S3, S6, and S12 have different locations in comparison to Figs. 8, 9, and 10.

Additionally, based on studies of stress drop and rupture length by Ciardelli and Assumpção (2019), it is possible for a 2.9 mR earthquake to have a rupture size of 1 km in length. However, this would require a very low stress drop of about 0.1 MPa, which is ten times smaller than the average stress drop in Brazil, according to the authors, i.e. assuming no significant variations between the local magnitude mR and the moment magnitude Mw.

In other words, Sete Lagoas sequence seems to result from a more complex fault system than just a one singular rupture. Based on the literature, similar waveforms may indicate the proximity of the seismic source (Gao et al., 2021) and/or similarity in focal mechanisms (Kilb and Rubin, 2002), but it does not necessarily imply that the events share the same fault rupture.

Second hypothesis:

However, a new possibility arises if we exclude events that have a large azimuthal gap ($> 170^o$), which can introduce high uncertainties in the location results. **Tab. 5.2** presents some inversion parameters obtained from the relocation using a combination of P, S, and
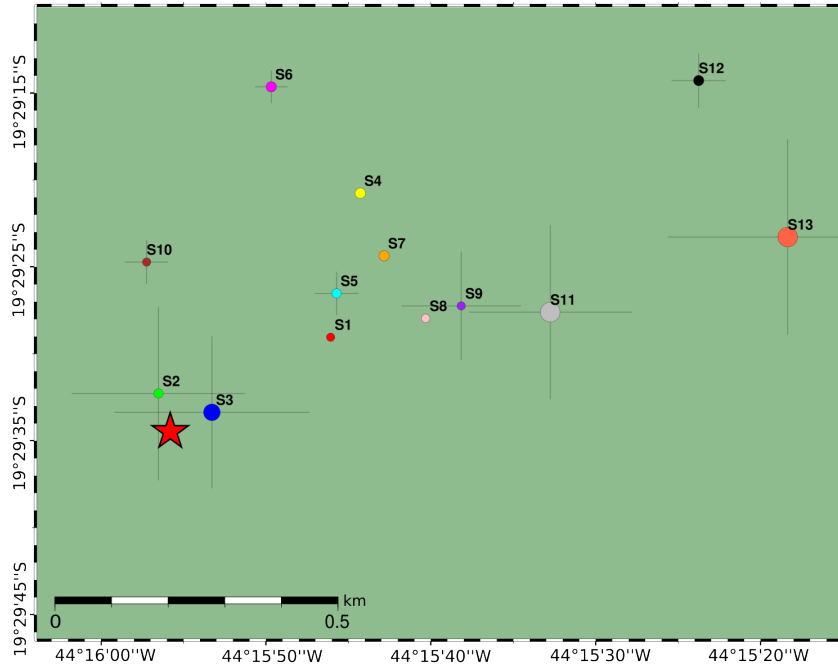
Figure 5.10: Location of Sete Lagoas events. Red star is the reference (Master) event and circles the located target events using only Lg-waves with the HYPOSAT code. This type of location has no depth determination.

Lg-waves.

Table 5.2 - Relocation parameters from combination of P, S and Lg-waves. The parameters are: Event number (Ev n°); Date and hour; magnitude (mag); depth in km; Azimutal gap (GAP °); inversion root mean square (rms) travel time residual; H.er (horizontal error average in km); V.er (vertical error in km). These events are shown in Fig. 5.8.

Ev n	Date - hour	mag	Depth	GAP	rms	H.er	V.er
S1	2022/05/08 - 10:49:1.03	2.0	1.08	172	0.011	0.06	0.11
S2	2022/05/16 02:17:38.76	2.1	0.99	137	0.028	0.16	0.35
S3	2022-05-20 - 22:36:31.45	2.7	0.95	172	0.021	0.12	0.20
S4	2022-05-29 - 20:33:44.28	2.2	1.21	137	0.015	0.04	0.19
S5	2022-05-30 - 15:01:50.06	2.1	1.02	137	0.017	0.30	0.22
S6	2022-05-31 - 00:39:1.06	2.2	0.88	137	0.031	0.16	0.38
S7	2022-06-01 - 03:17:34.39	2.2	1.02	172	0.026	0.15	0.25
S8	2022-06-06 - 13:49:11.74	2.0	1.17	172	0.009	0.05	0.09
S9	2022-06-27 - 08:16:39.18	2.5	1.15	90	0.031	0.08	0.28
S10	2022-07-25 - 14:56:8.88	2.2	1.02	91	0.014	0.06	0.16
S11	2022-07-29 - 20:44:52.17	2.9	0.93	91	0.031	0.06	0.30
S12	2022-11-24 - 02:02:36.52	2.2	1.08	90	0.045	0.19	0.55
S13	2022-12-28 - 03:42:30.83	2.9	0.88	90	0.060	0.18	0.54

Continues on the next page. . .

Tabela 5.2 - Continuation

Ev n	Date - hour	mag	Depth	GAP	rms	H.er	V.er

By selecting the events S2, S4, S5, and S9 13 (that is excluding all events with a gap 140 deg.), we can construct the (261°, 50°) plane, as depicted in **Fig. 5.11**. This plane exhibits a rupture length (L) of 1000m, trending WSW-ENE, and dipping towards the NNW.
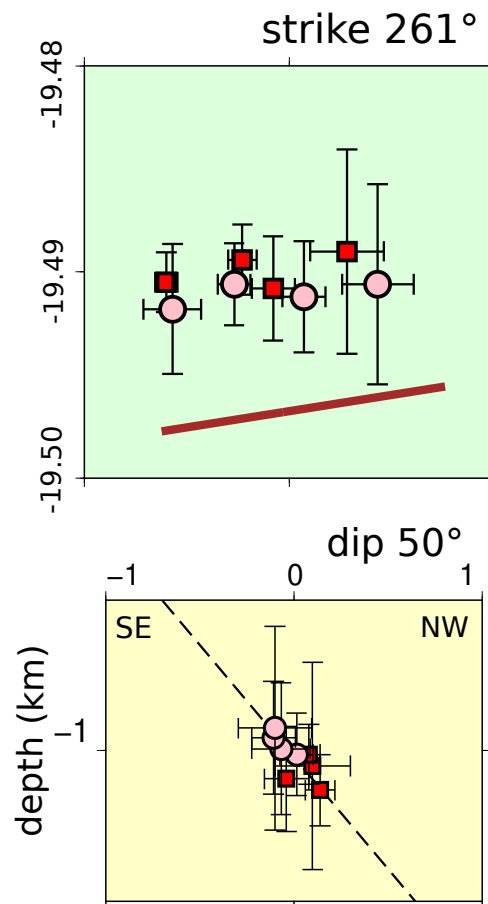

Figure 5.11: The SW-NE trend is established by excluding events with a high azimuthal gap. The trend dips 50° to the NW. Pink circles represent depths less than 1.1 km, while red squares represent depths greater than 1.1 km.

To differentiate between the two hypotheses proposed here, it is necessary to continue monitoring the aftershocks. This ongoing monitoring will allow us to observe if the events maintain similar waveforms and if they continue to exhibit spatial separation from the

mainshock. In addition to the location study, conducting a focal mechanism analysis using local stations would provide valuable insights into any potential connections or variations in the source rupture among the events. At any rate, the probable WSW-ENE (261°, 50°)trending fault plane can be used to help determine a focal mechanism by modelling the regional surface waves.

# Chapter 6

Cajati sequence

The Cajati region in São Paulo state has been affected by a series of suspected induced earthquakes related to the mining of carbonate rocks for fertilizer production. The largest earthquake occurred in 2015, with a magnitude of 3.3 mR **Fig. 6.1**. Since then, the region has experienced several earthquakes/microseisms due to mining activities. These facilities are part of the Cajati Mining and Chemical Complex, located near the city of Cajati, which has been involved in mineral exploration in the area since 1943 (Faleiros and Pavan, 2013). Here, we will analyze some earthquakes recorded by the regional RSBR stations, as shown in **Tab. 6.1**.

Table 6.1 - Some large earthquakes that occurred near the city of Cajati-SP between 2009 and 2022. The numbers correspond to the relocated events. The epicenters were obtained from the Seismic Bulletin of IAG-USP. Events without epicenters were recorded by one single station and have large uncertainties. The numbers correspond the numbering assigned to each of these relocated events.

N° evt	Date - hour	Latitude	Longitude	Magnitude (mR)
	2022/07/15 - 21:12:26	-24.66	-48.17	2.3
	2020/07/23 - 14:23:12	-24.80	-48.06	2.0
C5	2020/04/16 - 16:59:51	-24.72	-48.08	2.1
	2019/08/20 - 12:23:47	-	-	1.9
	2019/08/01 - 17:20:32	-	-	1.6
C4	2019/01/31 - 08:22:34	-24.73	-48.14	2.8
	2018/09/22 - 12:21:58	-	-	1.1
	2018/06/05 - 20:22:47	-24.82	-48.05	2.3
C3	2018/05/25 - 21:16:33	-24.72	-48.11	2.8
C2	2016/11/18 - 06:34:21	-24.78	-48.13	2.4
C1	2016/05/20 - 23:27:23	-24.74	-48.11	2.7
M	2015/10/23 - 06:53:11	-24.73	-48.12	3.3
	2009/06/08 - 17:16:04	-24.74	-48.12	2.9

The events exhibit a wide temporal distribution. There are many other events that cannot be recorded by the RSBR due to their low magnitudes. **Fig. 6.2** shows the location

of numbered events made by USP Seismological Center, the epicenters are offset from the bottom of the mine pit (gray area) due to the lack of accuracy in the localization. However, studies conducted by Dias (2022) using the local network of the mining company between 2019-2021 identified approximately 2.972 seismic events concentrated in the vicinity of the open pit **Fig. 6.3**. The author discovered that out of 30 events with a local magnitude higher than 0 ML, 22 (73%) are situated within the area of greatest concentration, which aligns with the bottom of the pit.
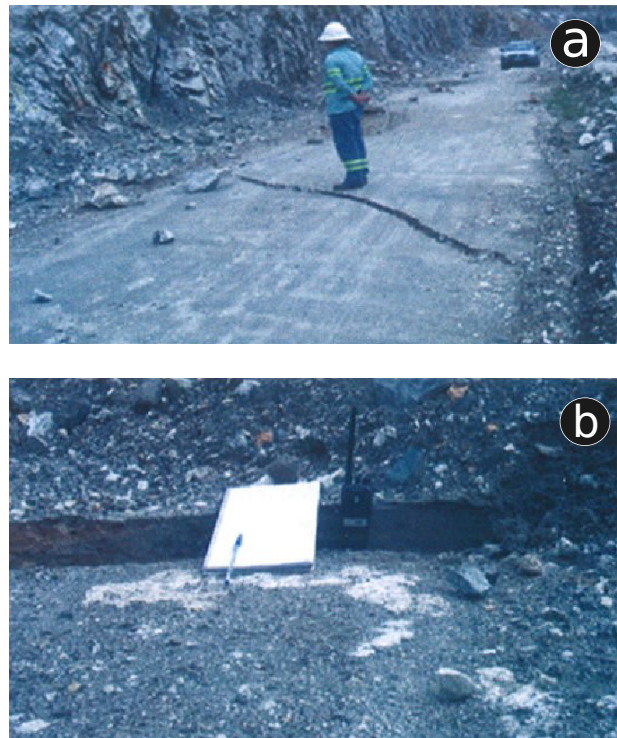
Figure 6.1: Transverse fracture view resulting from a magnitude 3.3, 2015-10-23 earthquake on the slope of the Cajati mine. a) Perspective of one of the slopes. b) Close-up view showing the displacement between the blocks, Coppedê (2018).
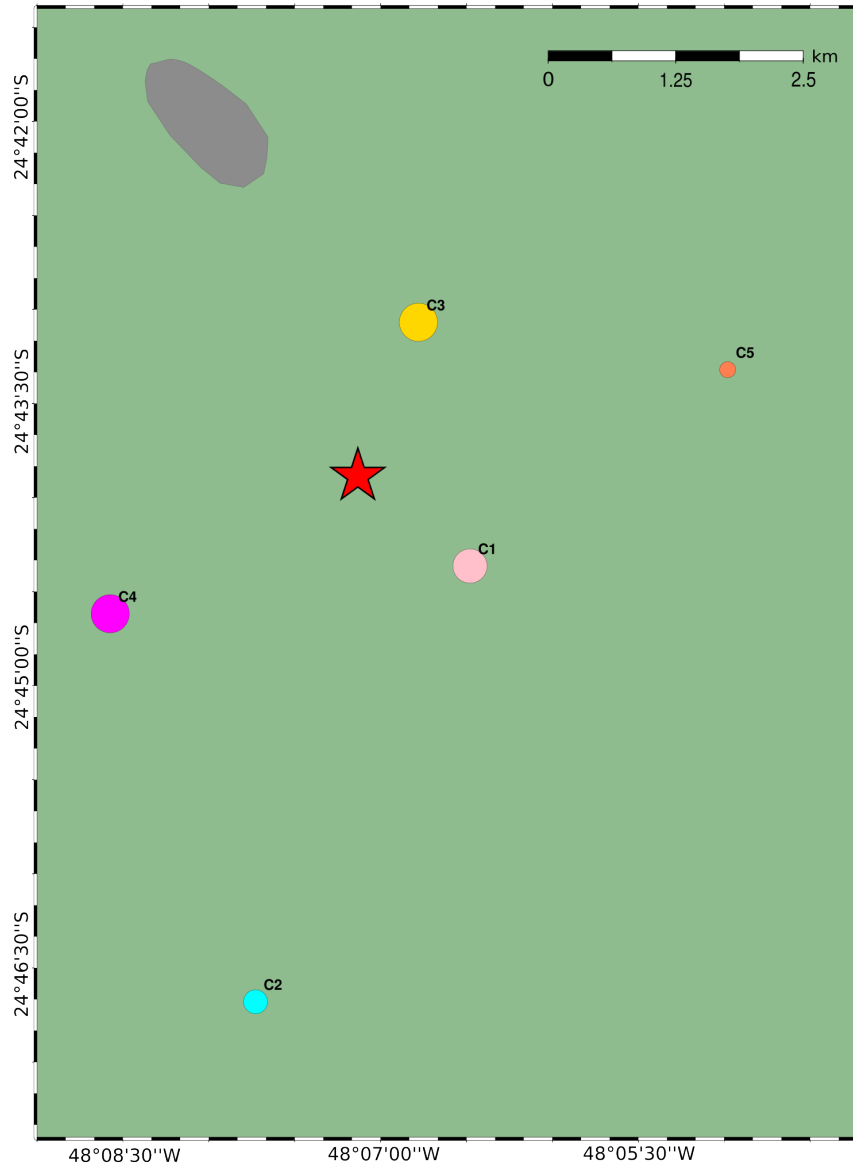
Figure 6.2: Absolute location made by USP seismological Center. The gray area represents the mine pit or excavation site. We do not recognize any epicenter alignment, and the location error can be up to 10 km.

The waveforms of the relocated events can be observed in **Fig. 6.4**, **6.5**, **6.6** and **6.7**. Some of the waveforms do not appear to be very similar, mainly due to the low signal-to-noise ratio. This is particularly noticeable with C1 and C2 events on TIJ01, as well as C5 on FRTB station. Additional figures from Cajati S-waves correlation can be found in the Appendix (**section C**).
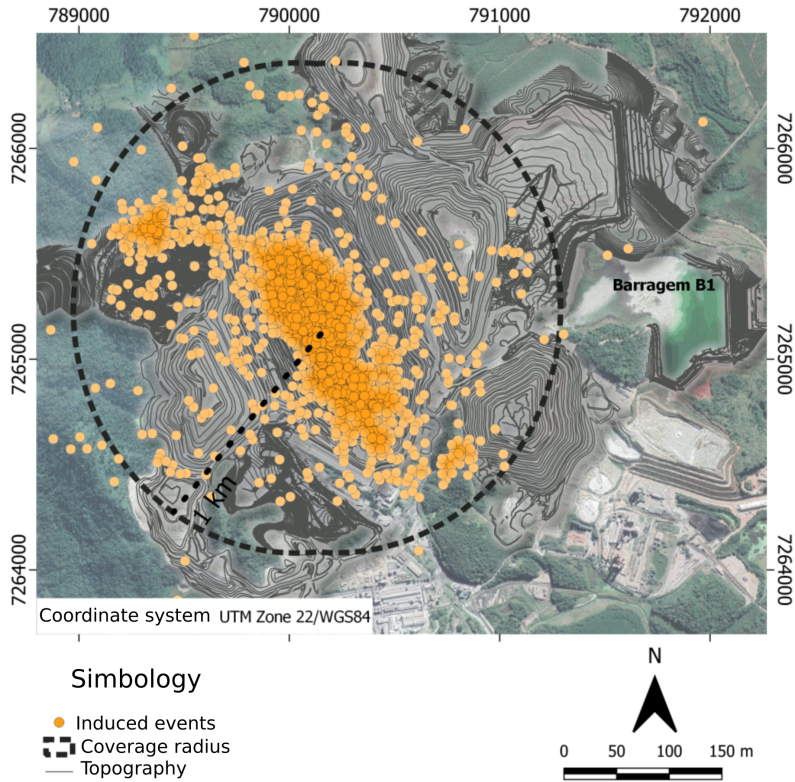
Figure 6.3: Location of induced seismic events by mining activities. Showed that most part of seismic events were concentrated within a radius of 1 km from the bottom of the mining pit, adapted from Dias (2022).
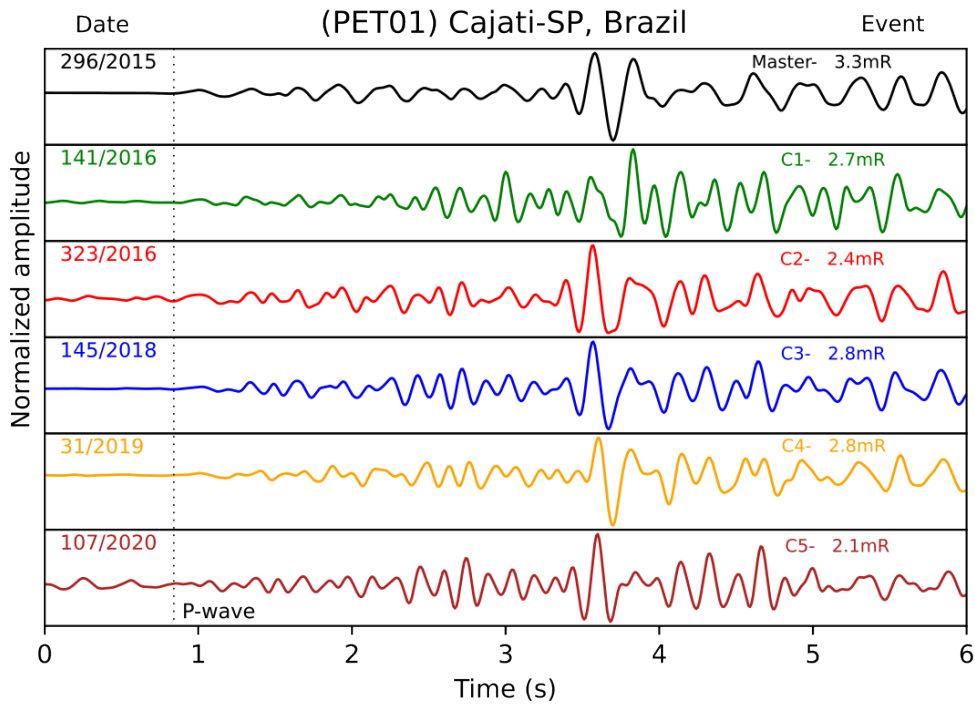

Figure 6.4: Waveforms of the mainshock and five relocated aftershocks near Cajati showing a noticeable similarity. ON.PET01 station (98km), vertical component velocity records, band-pass filtered (2-8Hz). The event times (day of year/year) are displayed in the left corner, while the event number and magnitude are shown in the right corner. The dashed line indicates the P-wave arrivals.
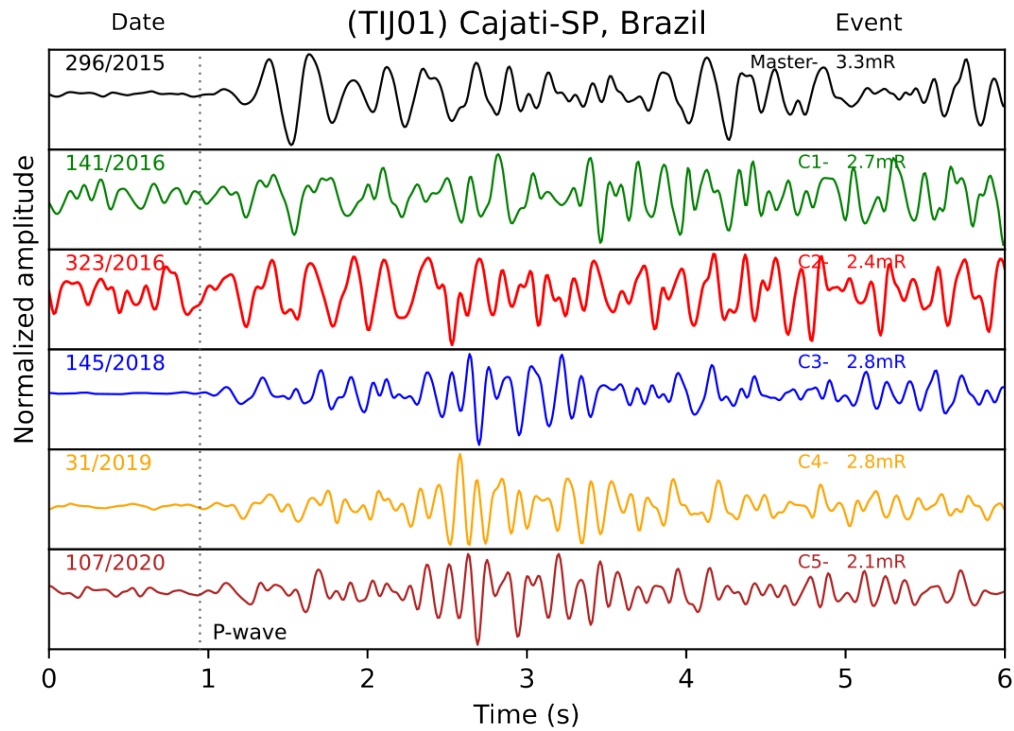
Figure 6.5: P waveforms of ON.TIJ01 station (160km), vertical component, velocity records band-pass filtered (2-8Hz).
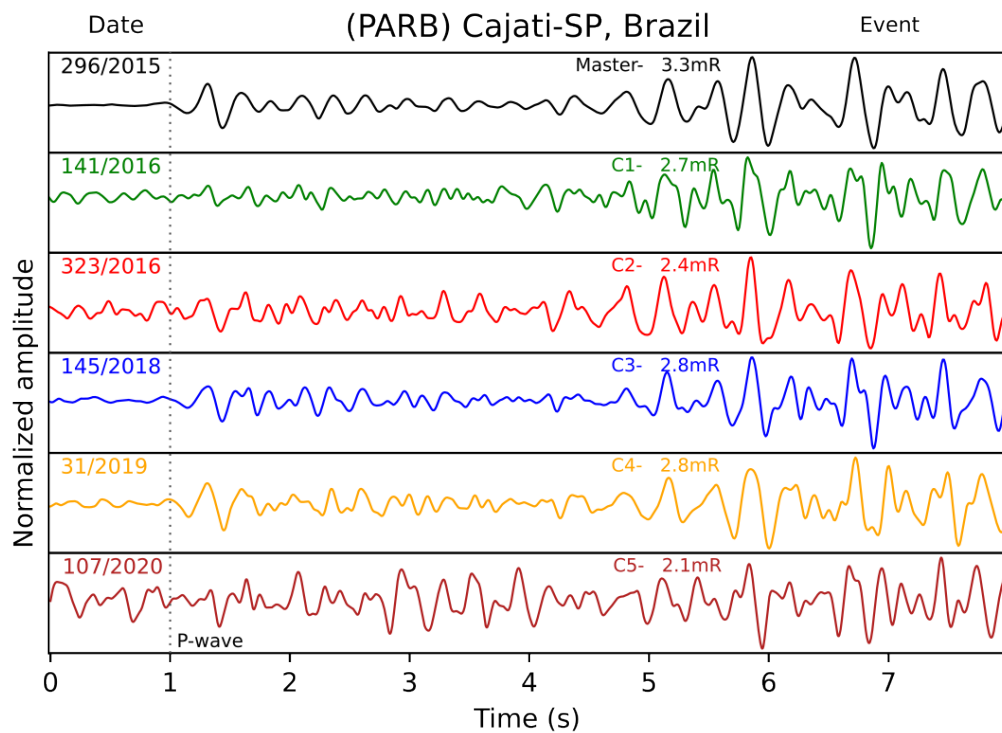

Figure 6.6: P waveforms of BL.PARB station (296km), vertical component, velocity records band-pass filtered (2-8Hz).
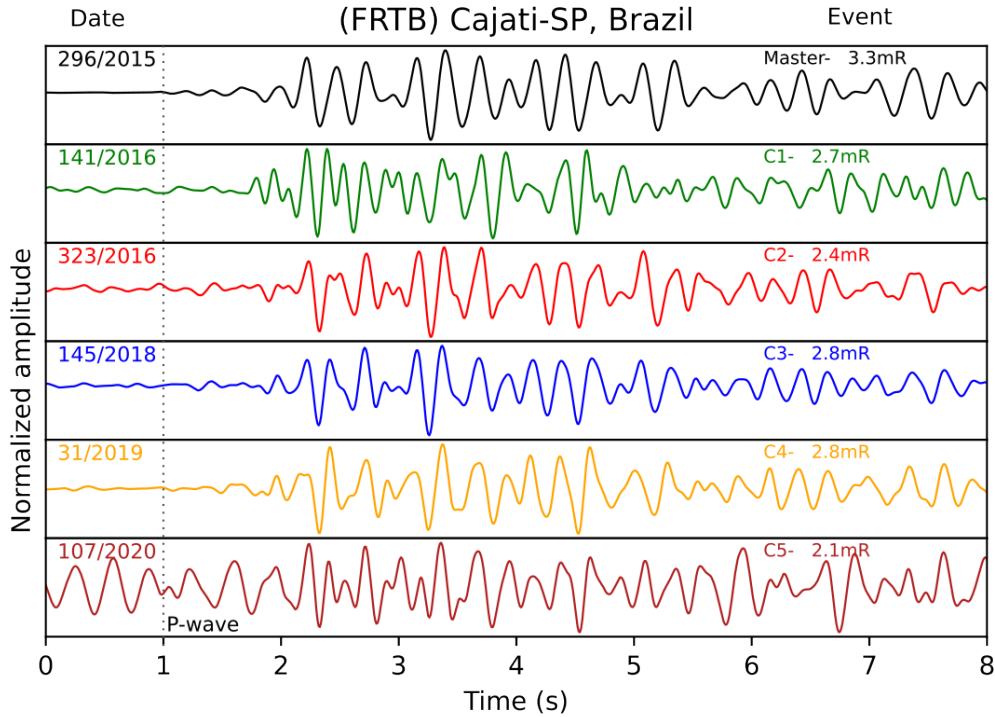
Figure 6.7: Pn waveforms of BL.FRTB station (212km), vertical component, velocity records band-pass filtered (2-8Hz).

The earthquakes believed to be induced are a result of the exploration of carbonatites from the alkaline rocks within Jacupiranga Complex, a Mesozoic magmatic intrusion characterized by an elliptical shape and an NNW-SSE orientation, as described by Barros (2001). The suite represents one of the various manifestations of alkaline magmatism that occur on the edge of the Paraná Basin, with an age of 131 $\pm$ 3 Ma (Amaral et al., 1976); (Roden et al., 1985).

According to Alves and Hagni (2008), drilling has provided evidence that the carbonatites facies extend to a depth of at least 400 m below sea level. These structures exhibit a general dip angle of 80° and are primarily represented by a shear zone (fault). The carbonatites in the area exhibit various structural elements, including joints, faults, dikes, and fluid structures. These elements are arranged in a radial and concentric pattern, indicating the presence of an intrusive body formed by five successive intrusions (Barros, 2001); (Alves and Hagni, 2008).

To investigate the potential relationships between mining activity and seismic occurrences, we will relocate the events highlighted in **Tab. 6.1** and compare them with the results obtained by (Dias, 2022) using a local network.

6.1 Relative location

6.1.1 Rayleigh time shift method

Using the Lg-wave phase velocity of 3.1 km/s, which is the same as the Sete Lagoas sequence due to similarities in rock physics. The event that occurred on October 23, 2015, with a magnitude of 3.3 (mR), was selected as the reference for the analysis. **Fig. 6.8** displays the compiled results obtained from the inversion of the surface wave sinusoidal equation (2.3).
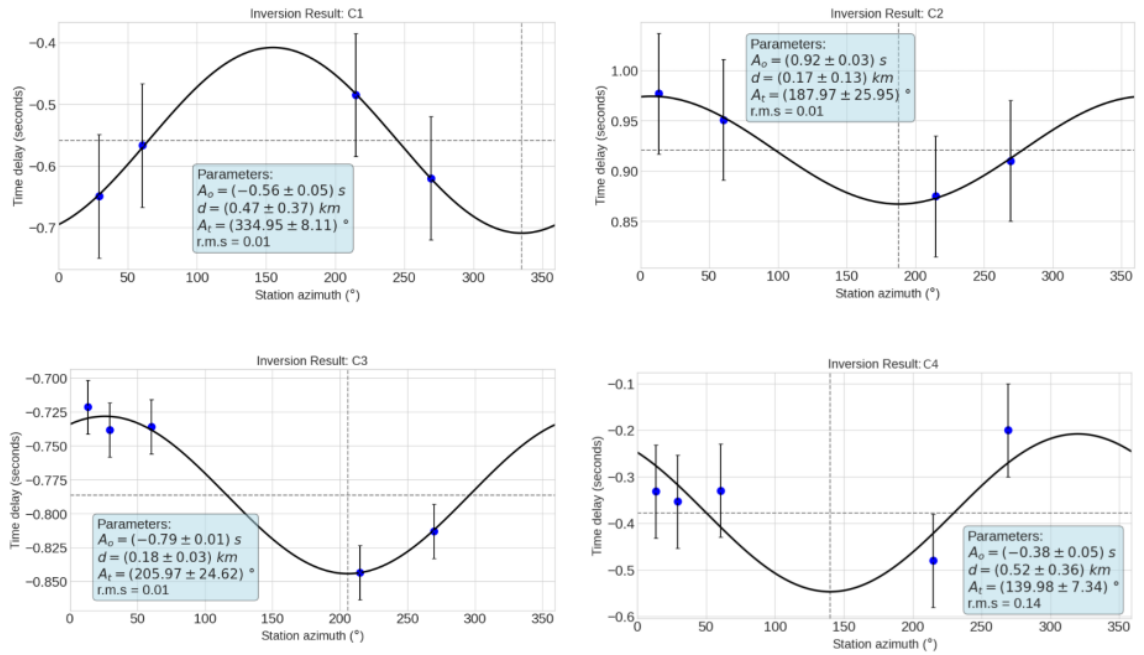
Figure 6.8: Fitted curve for the Lg relative location of the aftershocks (C1-C4). The solid line represents the best fit, and the blue points represent the time shift measurements with their associated error. The light blue box displays the inverted parameters and their respective errors. The vertical dashed line indicates the azimuth (At) of the target event relative to the master event. Note the high uncertainties in the distance (d) parameter by C1, C2 and C4.

For the case of Cajati, the standard deviation of eq. (2.5) was increased, due to the low SNR, particularly in observing surface waves, which should reflect an increase in parameter uncertainties. From **Fig. 6.8**, we can observe that we have increased the standard deviation, specially for events C1 ($\sigma_o = 0.2$) and C2 ($\sigma_o = 0.13$). Previously, we were using $\sigma_o = 0.03$ for Sete Lagoas and Amargosa. The adjust of standard deviation is based on the stability of the waveform correlation when shifting the correlation window and applying filtering. If the pick adjustment, as described in section (2.2.1) remains

stable, the standard deviation (σ_o) is low. However, if it varies, the standard deviation becomes high. Additionally, the Cajati sequence suffers from limited azimuthal coverage, with nearby stations concentrated at similar azimuths, such as ON.PET01 (98km, 57°) and G.SPB (160km, 28°), resulting in significantly greater imprecision compared to previous sequences.
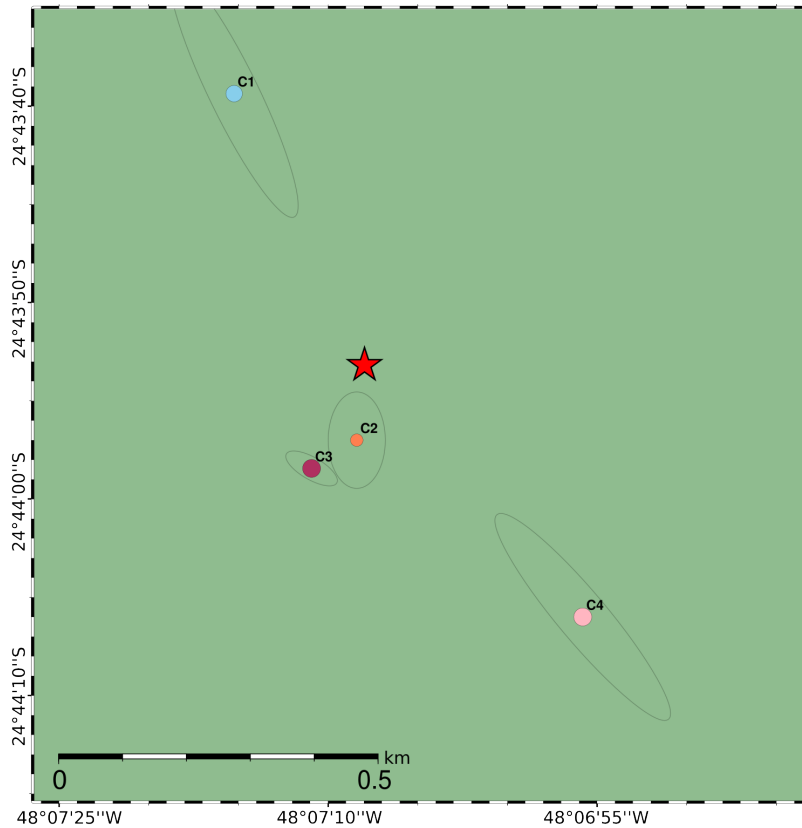

Figure 6.9: Location of Cajati events. Red star is the reference (Master) event and circles the located target events using Lg waves only Eq. (2.3). This type of location has no depth determination.

Fig. 6.9 shows the map results of the inversions using Rayleigh waves through Eq. (2.3).

6.1.2 *Relative location with Lg + P, S-waves, station correction method*

Similarly, as in the previous chapters, **Fig. 6.10**, **6.11**, and **6.12** represent the location using the station correction method (section 2.1) by incorporation the arrivals of both P- and S-waves. However, unlike the agreement observed in the previous chapters, the results do not seem to have a clear correlation. We will discuss each of them individually.
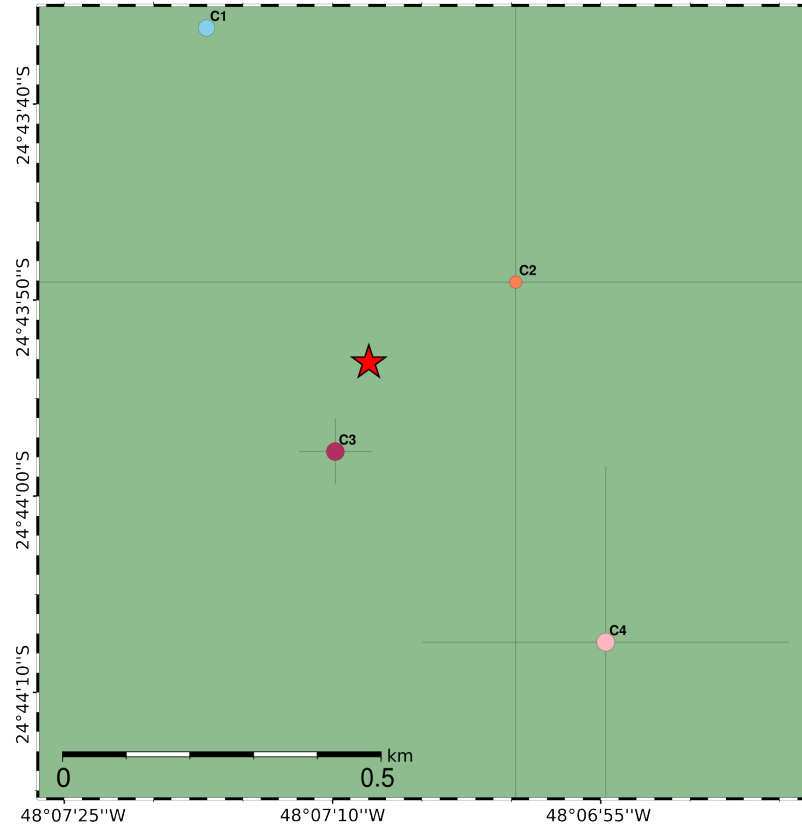
Figure 6.10: Location of Cajati events. Red star is the reference (Master) event and circles the located target events using only Lg-waves as described in section 2.1 . This type of location has no depth determination.

According to **Fig. 6.9**, we observe a NW-SE trend. Events C1 and C4 are located approximately 500m from the main event, but the uncertainties are high. Using this method, we were unable to locate the event of 2020 (C5), which had a lower magnitude (2.1 mR). By adjusting the standard deviation (σ), we observe that the main uncertainties lie in the radial direction (**Fig. 6.8, 6.9**), which coincides with the distance between the aftershocks C1 and C4 in relation to the other location results **Fig. 6.11** and **6.12**. On the other hand, the uncertainties in the azimuthal parameter (A_t) remained low.

In theory, the epicenters of map (**Fig. 6.10**) should coincide with the epicenters of the **Fig. 6.9** map, since both locations use only Lg surface waves (which do not determine the depth). Comparing them, the epicenters C1, C3, and C4 agree well, but event C2 is displaced by about 200m. The high errors observed for C2 can be attributed to the limited number of observations available for this event, which is based on only three data points. This lack of data can significantly impact the accuracy and precision of the localization results. Consequently, the discrepancies between the two methods and the large errors
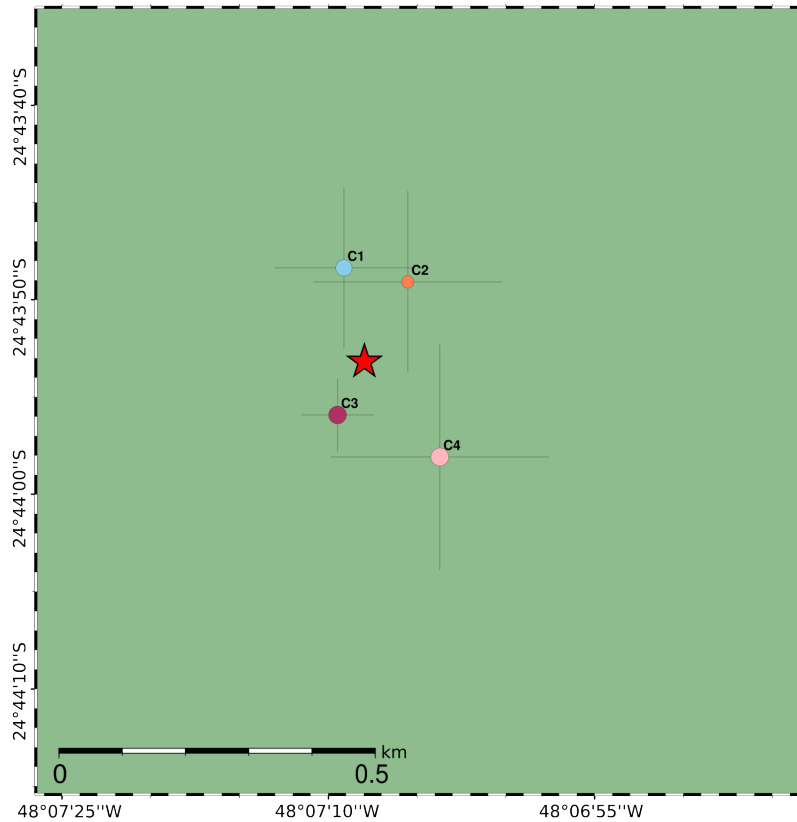
Figure 6.11: Location of Cajati events. Red star is the reference (Master) event and circles the located target events using P-, S- and Lg-waves. The reference event has is depth fixed in 1km, this type of location can determine the depths of the target events.

observed in **Fig. 6.10**, suggest that relying solely on surface waves for the localization of event C2 may not provide accurate results.

Compared to the other two locations, all events are closer to the reference event (2015), with C1 and C4 being displaced by approximately 300m. Additionally, a rough NW-SE trend can be observed. Furthermore, by incorporating the body waves along with the surface phases, the C1 and C4 events are brought even closer to the mainshock (**Fig. 6.11**).

Body waves are the easiest to observe for this sequence, making this location the most trustworthy among the four presented here. The map in **6.12** shows a clear NW-SE trend consistent with the mine pit. It is the only one where we can include the 16/04/2020 event (C5). The uncertainties are smaller. However, no fault plane could be determined. The clear NW-SE trend corresponds to the results of Dias (2022) (**Fig. 6.3**), following the orientation of the mine pit. Event C1 changes quadrant and is displaced by approximately 700m compared to its position in **Fig. 6.9**, **6.10**.
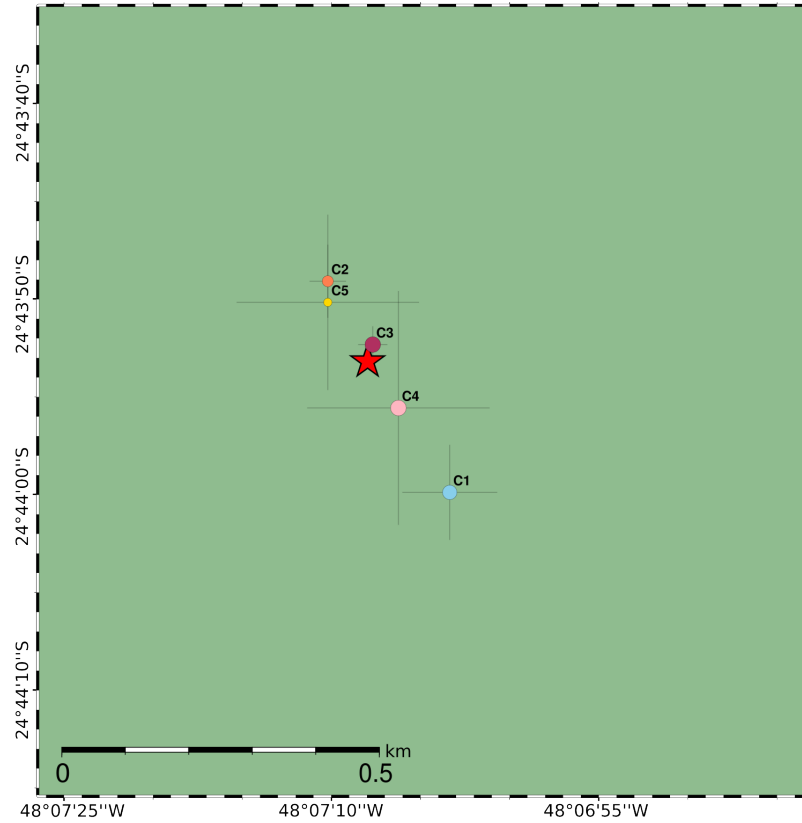
Figure 6.12: Location of Cajati events. Red star is the reference (Master) event and circles the located target events using only P- and S-waves. this type of location can determine the depths of the target events. Clear NW-SE trend, consistent with the pit of the mine.

For all maps of relocated events, there is a significant displacement compared to the epicenters determined by absolute location (**6.2**), with up to 6 km shift for event C2. So far, we do not have a clear explanation for the location discrepancies happening in the Cajati sequence. One possibility could be the low SNR, observed mainly for events C1, C2 on TIJ01 station, and C5 on PARB station. Since we have few available stations, the final results can be greatly influenced by these measurements. The discrepancies between the sinusoidal locations in **Fig. 6.9** and the location using body waves only, in **Fig. 6.12**, mainly occur in the radial direction, which is consistent with the high uncertainties for distance (d) parameter (**Fig. 6.8**). Another possible explanation could be clock issues with the stations managed by the National Observatory (ON), such as ON.PET01 or ON.TIJ01, which are the two closest stations to the epicentral area.
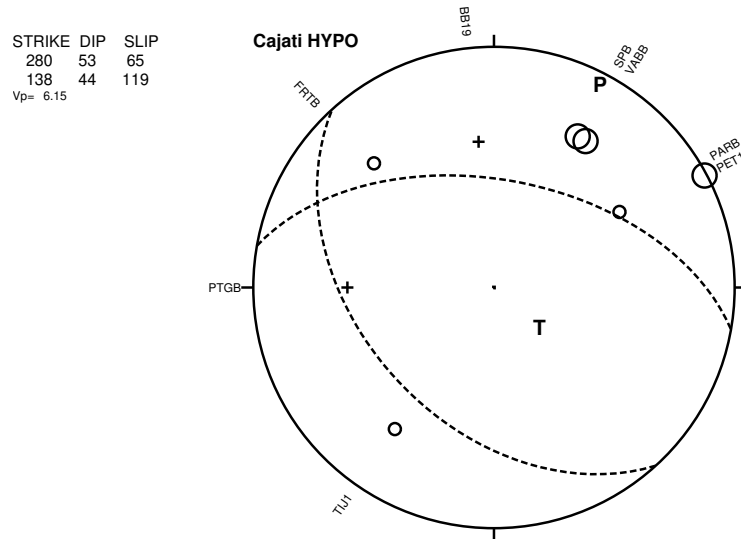
Figure 6.13: Possible fault plane solution by first-motion P-wave polarities using NW-SE nodal plane. Crosses represent compression, circles dilation. The size of the symbols corresponds to the quality of the data.

6.2 Focal mechanism

The regional stations do not provide enough reliable polarities to determine the focal mechanism. **Fig. 6.13** shows a possible fault plane solution using one nodal plane oriented NW-SE (280°, 53°, 65°) according to the alignment of the relative epicenters by body waves in **Fig. 6.12**. A reverse fault mechanism with NE-SW oriented P-axis is suggested. More studies are necessary to complete the focal mechanism, such as waveform modeling. The NW-SE orientation of the rupture plane will be a valuable information to constrain the focal mechanism.

Chapter 7

Conclusions

Four seismic events were analyzed using two distinct and independent methods of relative location, namely the station correction method and Rayleigh time shift. Both methods involve waveform cross-correlation. Based on this analysis, we were able to accurately determine the aftershocks of these seismic sequences using one of the events as a reference. Precise determination of these events of the sequence allowed us to study some source characteristics.

For Guyana, using the mainshock as the target and the largest aftershock as the reference, we recovered the NW-SE trend observed by satellite. Additionally, we relocated a 1965 event using global network stations and found it to be 50km southwest of the 2021 event, indicating that they did not occur in the same geological structure.

For Amargosa, the locations of the aftershocks showed a consistent pattern along a WNW-ESE trend with a rupture length of 1200m. We determined the focal mechanism through waveform modeling, which resulted in a moment magnitude (Mw) of 4.09, a depth of 1km, and a nodal plane orientation of (120°, 50°, 120°), indicating a reverse machenism and maximum horizontal stress (SHmax) parallel to the Brazilian coastline. We estimated a stress drop of 3.1MPa.

For Sete Lagoas, a total of 13 events were relocated, and two hypotheses were discussed: the apparent sparse distribution and the possibility of epicentral migration without a clear alignment. This suggests that each event could be an independent rupture; However, by excluding events with a large azimuthal gap, we were able to observe an ENE-WSW trend with a dip of approximately 50° to the northwest.

For Cajati, not all types of location methods yielded consistent results due to low SNR. The best location was obtained using only body waves, which showed a NW-SE trend

similar to the orientation of the major axis of the mine pit. This finding is consistent with the results of Dias (2022) who used local networks. Based on this trend, we determined the focal mechanism using P-wave polarities, which indicated a reverse fault with a nodal plane orientation of (280°, 53°, 65°).

Bibliography

Alves P. R., Hagni R. D., The carbonatite-hosted apatite deposit of Jacupiranga, Southeast Brazil-styles of mineralisation, ore characterisation and association with mineral processing , 2008

Amaral G., Mattos J. D., Almeida R., Cunha R., Paradella W., Carta geológica ao milionésimo da Folha de Belo Horizonte com base na Interpretação de imagens Landsat, IN. SBG, Cong, Bras. Geol, 1976, vol. 29, p. 229

Assumpção M., Ardito J., Barbosa J. R., An improved velocity model for regional epicentre determination in Brazil. In IV Simpósio Brasileiro de Geofísica , 2010, p. cp

Assumpção M., Dias F. L., Zevallos I., Naliboff J. B., Intraplate stress field in South America from earthquake focal mechanisms, Journal of South American Earth Sciences, 2016, vol. 71, p. 278

Barbosa J. S., Sabaté P., Geological features and the Paleoproterozoic collision of four Archean crustal segments of the São Francisco Craton, Bahia, Brazil: a synthesis, Anais da Academia Brasileira de Ciências, 2002, vol. 74, p. 343

Barbosa J. S. F., Sabaté P., Archean and Paleoproterozoic crust of the São Francisco craton, Bahia, Brazil: geodynamic features, Precambrian Research, 2004, vol. 133, p. 1

Barros G. d., Reavaliação geoestatística dos recursos/reservas de fosfato da Mina de Cajati, SP, Universidade de São Paulo, 2001, Ph.D. Thesis

Barros L. V., Assumpção M., Quintero R., Caixeta D., The intraplate Porto dos Gaúchos seismic zone in the Amazon craton—Brazil, Tectonophysics, 2009, vol. 469, p. 37

Berrocal J., Asssumpção M., Antezana R., Neto D., de Marins C., Ortega R., França H., Veloso J., sismicidade do Brasil, 1984

Bondár I., Myers S. C., Engdahl E. R., Bergman E. A., Epicentre accuracy based on seismic network criteria, Geophysical Journal International, 2004, vol. 156, p. 483

Brune J. N., Tectonic stress and the spectra of seismic shear waves from earthquakes, Journal of geophysical research, 1970, vol. 75, p. 4997

Brune J. N., Seismic sources, fault plane studies and tectonics, Eos, Transactions American Geophysical Union, 1971, vol. 52, p. IUGG

Bürgmann R., Rosen P. A., Fielding E. J., Synthetic aperture radar interferometry to measure Earth's surface topography and its deformation, Annual review of earth and planetary sciences, 2000, vol. 28, p. 169

Chiu K., Snyder D. B., Regional seismic wave propagation (Lg & Sn phases) in the Amerasia Basin and High Arctic, Polar Science, 2015, vol. 9, p. 130

Ciardelli C., Assumpção M., Rupture lengths of intraplate earthquakes in Brazil determined by relative location of aftershocks: evidence for depth dependence of stress drops, Journal of South American Earth Sciences, 2019, vol. 89, p. 246

Das S., Henry C., Spatial relation between main earthquake slip and its aftershock distribution, Reviews of Geophysics, 2003, vol. 41

Delouis B., FMNEAR: Determination of focal mechanism and first estimate of rupture directivity using near-source records and a linear distribution of point sources, Bulletin of the Seismological Society of America, 2014, vol. 104, p. 1479

Dias L. S. d. O., Monitoramento Microssísmico de uma Cava e Barragem de Rejeitos em Mineração - Estudo de Caso de Cajati/SP, Instituto de Geociências, Universidade Federal do Rio de Janeiro, Rio de Janeiro,, 2022, Tese (doutorado em geologia) - programa de pós-graduação em geologia, 173 p.

Ekström G., Global detection and location of seismic sources by using surface waves, Bulletin of the Seismological Society of America, 2006, vol. 96, p. 1201

Faleiros F. M., Pavan M., Geologia e recursos minerais da folha Eldorado Paulista SG. 22-XB-VI, 2013

Ferreira T. S., Caixeta J. M., Lima F. D., Controle do embasamento no rifteamento das bacias de Camamu e Almada, Boletim de Geociências da PETROBRAS, 2009, vol. 17, p. 69

Fonsêca J., Nascimento A., Bezerra F., Sousa M., Menezes E., Preliminary analysis of the 2020 Amargosa (NE Brazil) seismic activity. In 17th International Congress of the Brazilian Geophysical Society , 2021, p. X

Gao D., Kao H., Wang B., Misconception of waveform similarity in the identification of repeating earthquakes, Geophysical Research Letters, 2021, vol. 48, p. e2021GL092815

Geiger L., Herdbestimmung bei Erdbeben aus den Ankunftszeiten. Nachrichten von der Königlichen Gesellschaft der Wissenschaften zu Göttingen, Mathematisch-Physikalische Klasse, 331–349. 1912 transliterated in English by FWL Peebles & AH Corey: Probability method for the determination of earthquake epicenters from the arrival time only, Bulletin St. Louis University, 1910, vol. 8, p. 60

Hanks T. C., Kanamori H., A moment magnitude scale, Journal of Geophysical Research: Solid Earth, 1979, vol. 84, p. 2348

Howe M., Ekström G., Nettles M., Improving relative earthquake locations using surface-wave source corrections, Geophysical Journal International, 2019, vol. 219, p. 297

Kilb D., Rubin A. M., Implications of diverse fault orientations imaged in relocated aftershocks of the Mount Lewis, ¡¿M¡/i¿ ¡sub¿ ¡i¿L¡/i¿ ¡/sub¿ 5.7, California, earthquake, Journal of Geophysical Research: Solid Earth, 2002, vol. 107, p. ESE 5

Lienert B. R., Havskov J., A computer program for locating earthquakes both locally and globally, Seismological Research Letters, 1995, vol. 66, p. 26

Lima C., Nascimento E., Assumpção M., Stress orientations in Brazilian sedimentary basins from breakout analysis: implications for force models in the South American plate, Geophysical Journal International, 1997, vol. 130, p. 112

Michael Cleveland K., Ammon C. J., Precise relative earthquake location using surface waves, Journal of Geophysical Research: Solid Earth, 2013, vol. 118, p. 2893

Neto G. S. L., Julià J., Determination of intraplate focal mechanisms with the Brazilian Seismic Network: A simplified Cut-and-Paste approach, Journal of South American Earth Sciences, 2023, vol. 121, p. 104149

Rivadeneyra-Vera C., Assumpção M., Minaya E., Aliaga P., Avila G., Determination of the fault plane and rupture size of the 2013 Santa Cruz earthquake, Bolivia, 5.2 Mw, by relative location of the aftershocks, Journal of South American Earth Sciences, 2016, vol. 71, p. 54

Rivadeneyra-Vera C., Font Y., Bianchi M. B., P-and S-wave 3D velocity models for the South American platform, Brazilian Journal of Geophysics, 2021, vol. 39, p. 465

Roden M. F., Murthy V. R., Gaspar J. C., Sr and Nd isotopic composition of the Jacupiranga carbonatite, The Journal of Geology, 1985, vol. 93, p. 212

Santos J. O. S., Hartmann L. A., Gaudette H. E., Groves D. I., Mcnaughton N. J., Fletcher I. R., A new understanding of the provinces of the Amazon Craton based on integration of field mapping and U-Pb and Sm-Nd geochronology, Gondwana Research, 2000, vol. 3, p. 453

Schweitzer J., HYPOSAT–An enhanced routine to locate seismic events, Pure and Applied Geophysics, 2001, vol. 158, p. 277

Shirzad T., Safarkhani M., Assumpção M. S., Extracting reliable empirical Green's functions using weighted cross-correlation functions of ambient seismic noise in west-central and southern Brazil, Geophysical Journal International, 2022, vol. 230, p. 1441

Von Seggern D., Relative location of seismic events using surface waves, Geophysical Journal International, 1972, vol. 26, p. 499

Waldhauser F., A Double-Difference Earthquake Location Algorithm: Method and Application to the Northern Hayward Fault, California, Bulletin of the Seismological Society of America, 2000, vol. 90, p. 1353

Waldhauser F., Ellsworth W. L., Fault structure and mechanics of the Hayward fault, California, from double-difference earthquake locations, Journal of Geophysical Research: Solid Earth, 2002, vol. 107, p. ESE

Waldhauser F., Michele M., Chiaraluce L., Stefano R. D., Schaff D. P., Fault Planes, Fault Zone Structure and Detachment Fragmentation Resolved With High-Precision Aftershock Locations of the 2016–2017 Central Italy Sequence, Geophysical Research Letters, 2021, vol. 48

Wells D. L., Coppersmith K. J., New empirical relationships among magnitude, rupture length, rupture width, rupture area, and surface displacement, Bulletin of the seismological Society of America, 1994, vol. 84, p. 974

Appendix

Appendix A

Amargosa S-wave correlation
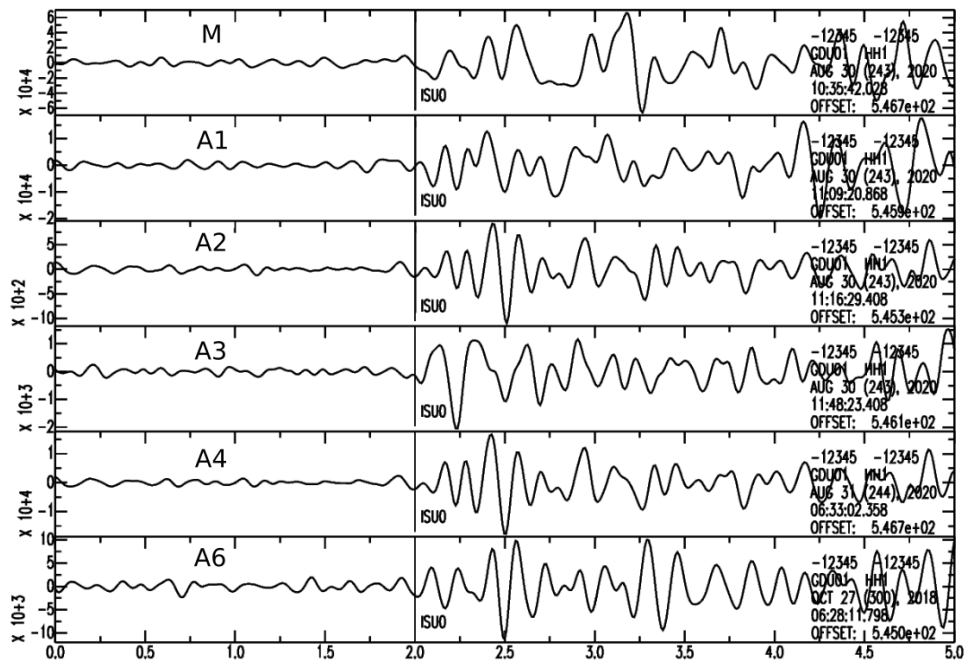
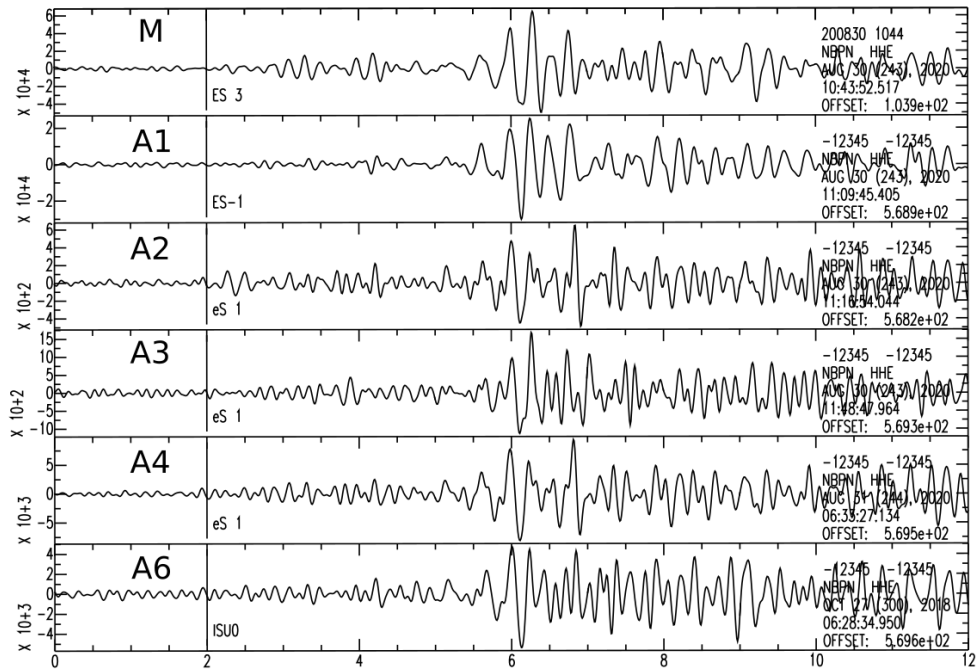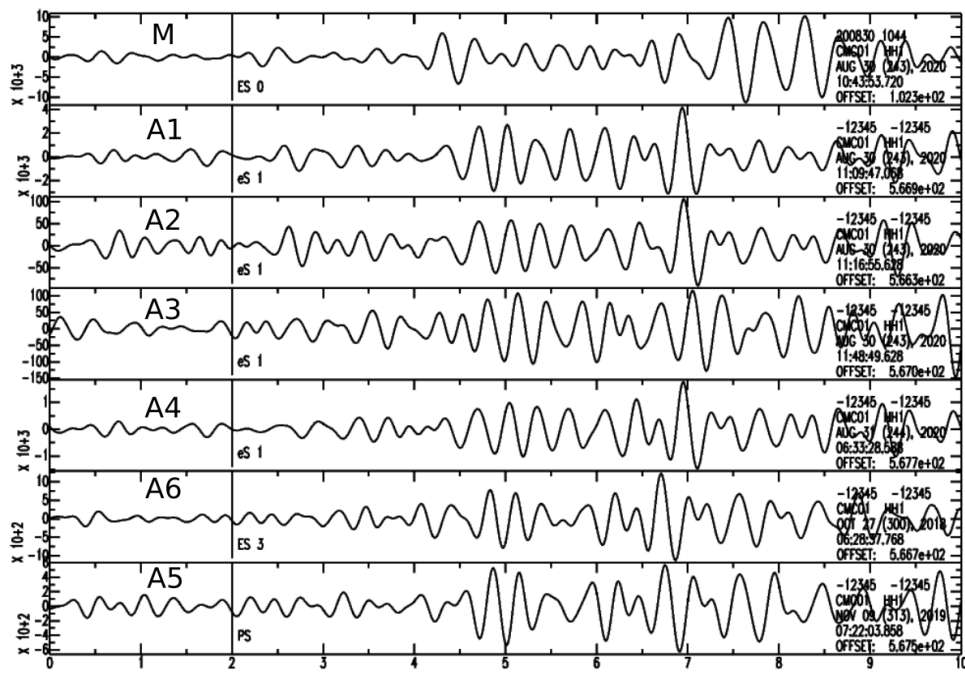*Figure A.1:* Waveforms correlation for S-wave on ON.GDU01 station (79km). HH1 component velocity records, band-pass filtered (2 - 8Hz). The event date and time are displayed in the left corner, while the event number are show in the right corner. The GDU01 station is highly sensitive to variations in focal mechanism and path due to its close proximity to epicenter location.
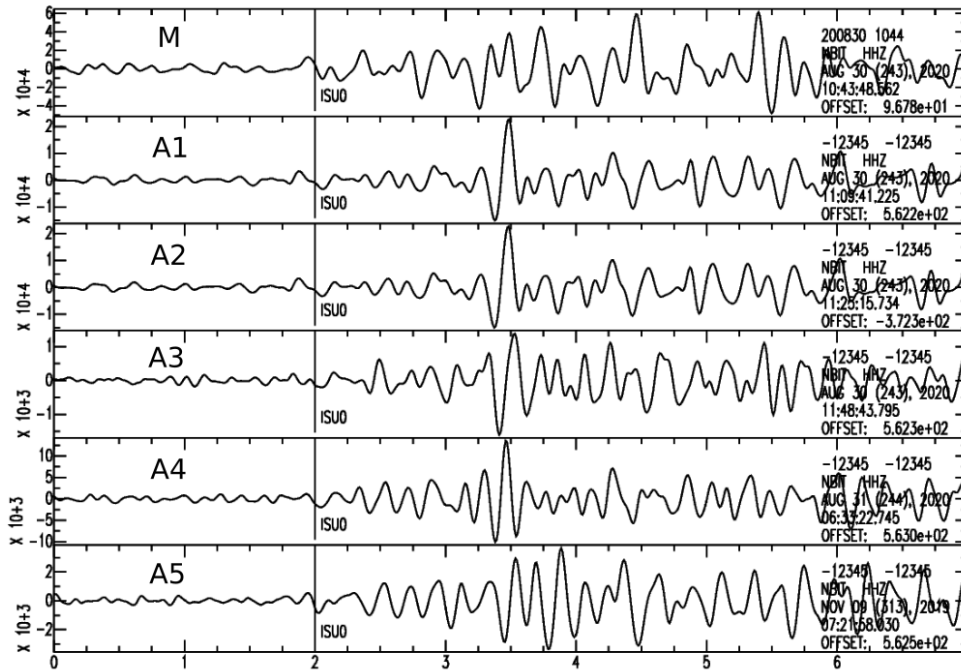
Figure A.2: Waveforms correlation for S-wave on ON.NBIT station (214km), HHZ component velocity records, band-pass filtered (2 - 8Hz).

Figure A.3: Waveforms correlation for S-wave on ON.NBPN station (248km), HHE component velocity records, band-pass filtered (2 - 8Hz).

Figure A.4: Waveforms correlation for S-wave on ON.CMC01 station (260km), HH1 component velocity records, band-pass filtered (2 - 4Hz).
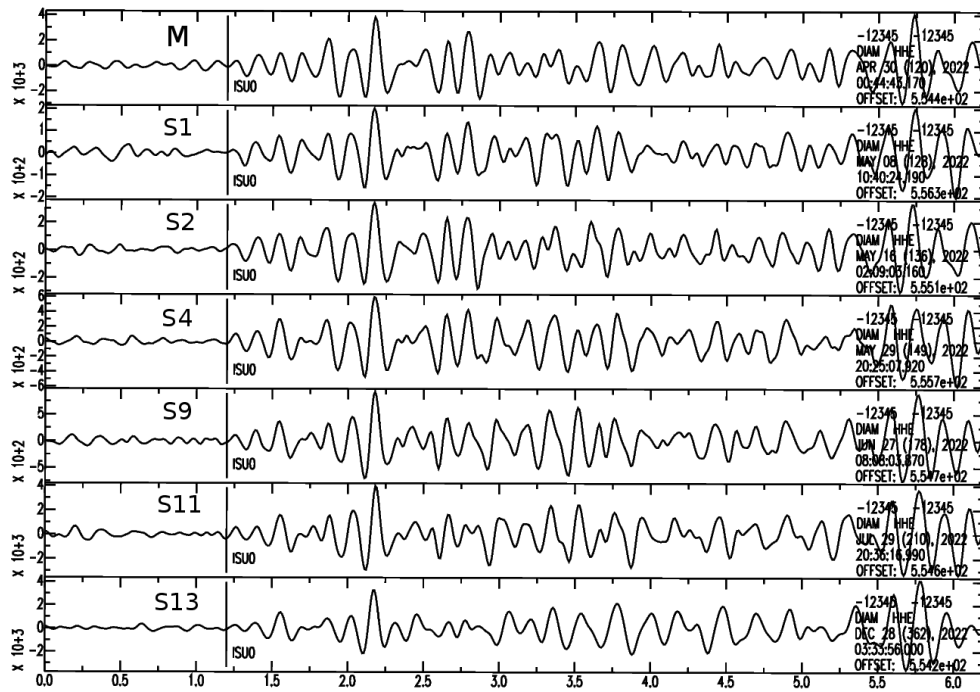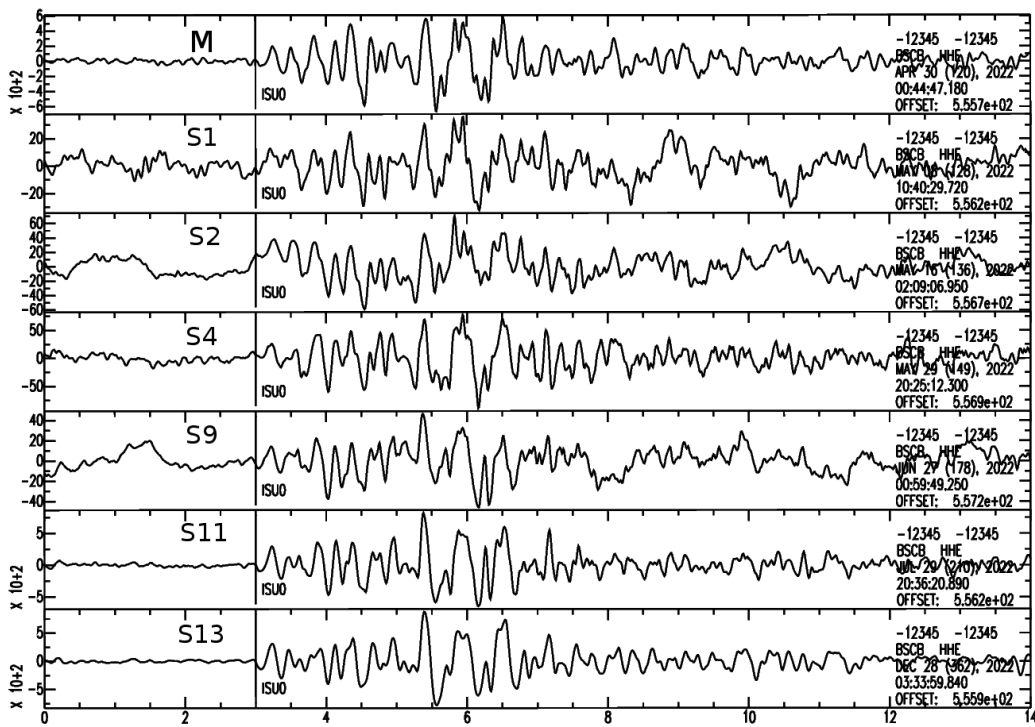
Appendix B

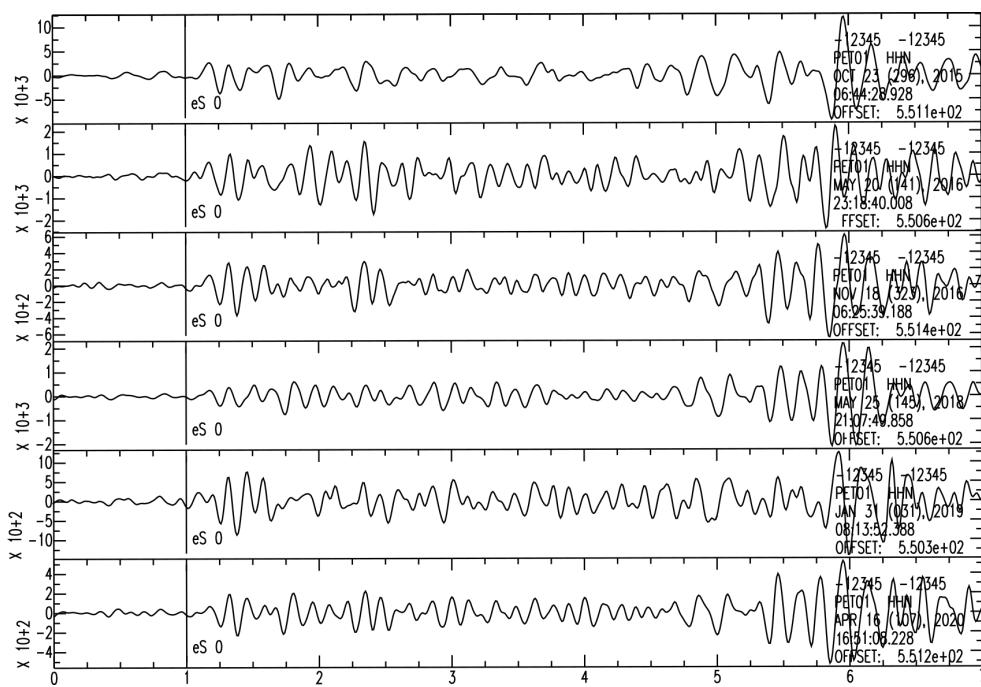## Sete Lagoas S-wave correlation

Figure B.1: Waveforms correlation for S-wave on BL.DIAM station (142km), HHE component velocity records, band-pass filtered (2 - 8Hz).

Figure B.2: Waveforms correlation for S-wave on BL.BSCB station (173km), HHE component velocity records, band-pass filtered (1 - 4Hz).

Appendix C

Cajati S-wave correlation

Figure C.1: Waveforms correlation for S-wave on ON.PET01 station, HHN component velocity records, band-pass filtered (2 - 8Hz).
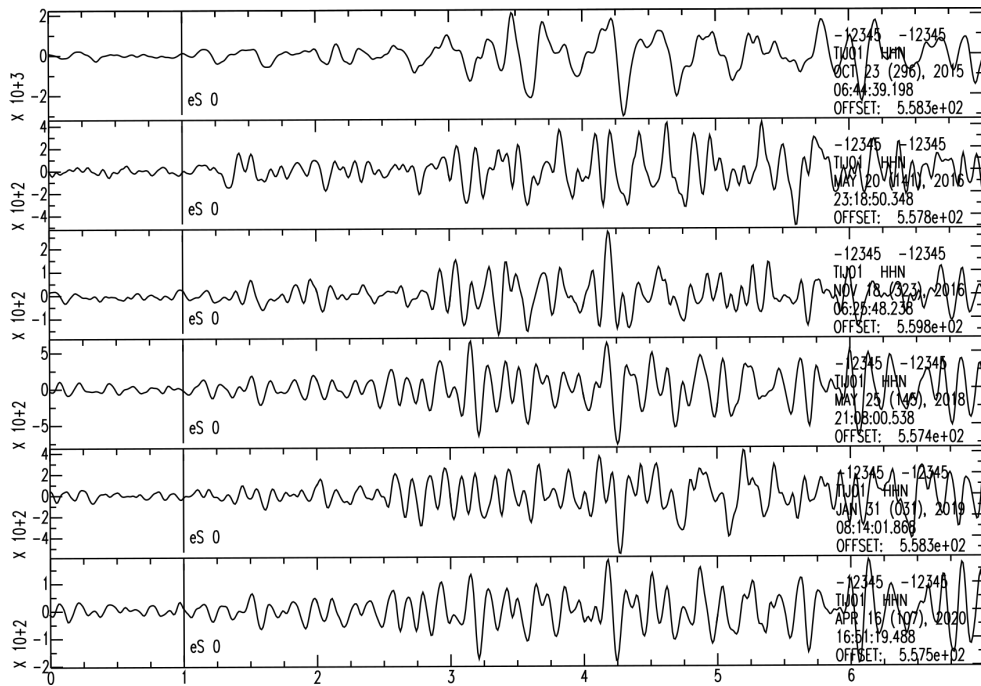
Figure C.2: Waveforms correlation for S-wave on ON.TIJ01 station, HHN component velocity records, band-pass filtered (2 - 8Hz).
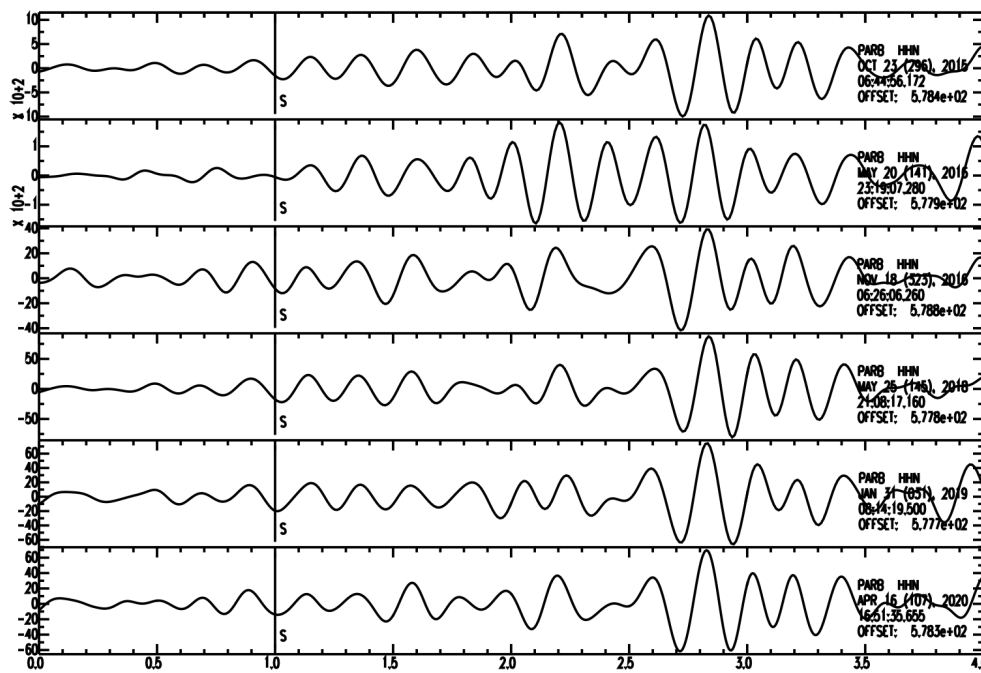

Figure C.3: Waveforms correlation for S-wave on BL.PARB station, HHN component velocity records, band-pass filtered (3 - 6Hz).
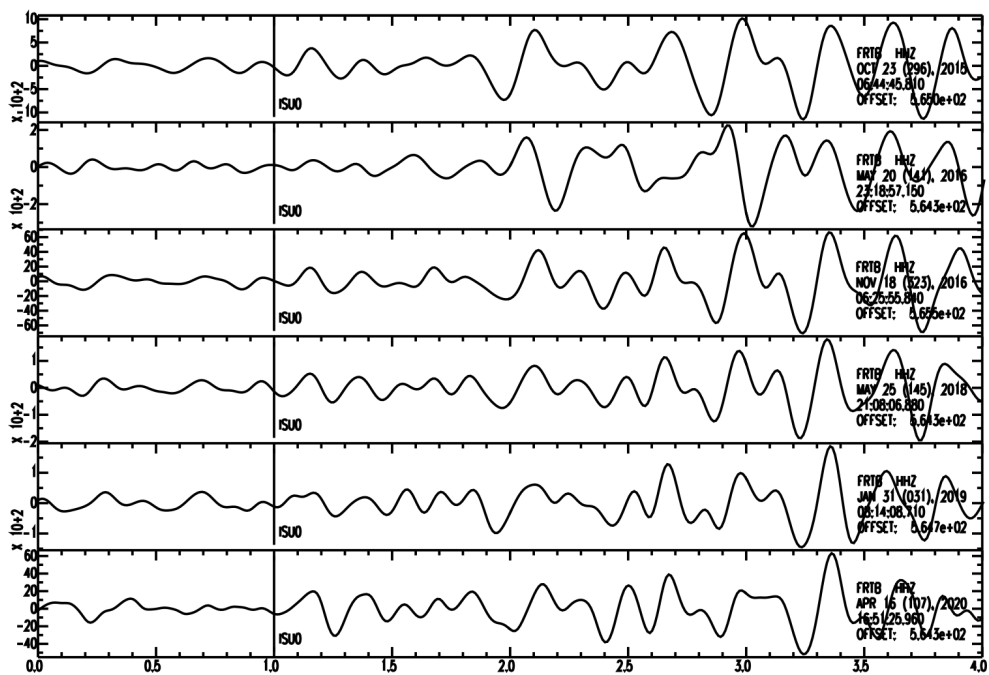
Figure C.4: Waveforms correlation for S-wave on BL.FRTB station, HHZ component velocity records, band-pass filtered (2 - 8Hz).